National Renewable Energy Laboratory
Innovation for Our Energy Future

A national laboratory of the U.S. Department of Energy
Office of Energy Efficiency & Renewable Energy

Lidar for Turbine Control

March 1, 2005 – November 30, 2005

M. Harris
QinetiQ Limited
Malvern, Worcestershire, United Kingdom

M. Hand, A. Wright
National Renewable Energy Laboratory
Golden, Colorado

Technical Report
NREL/TP-500-39154
January 2006

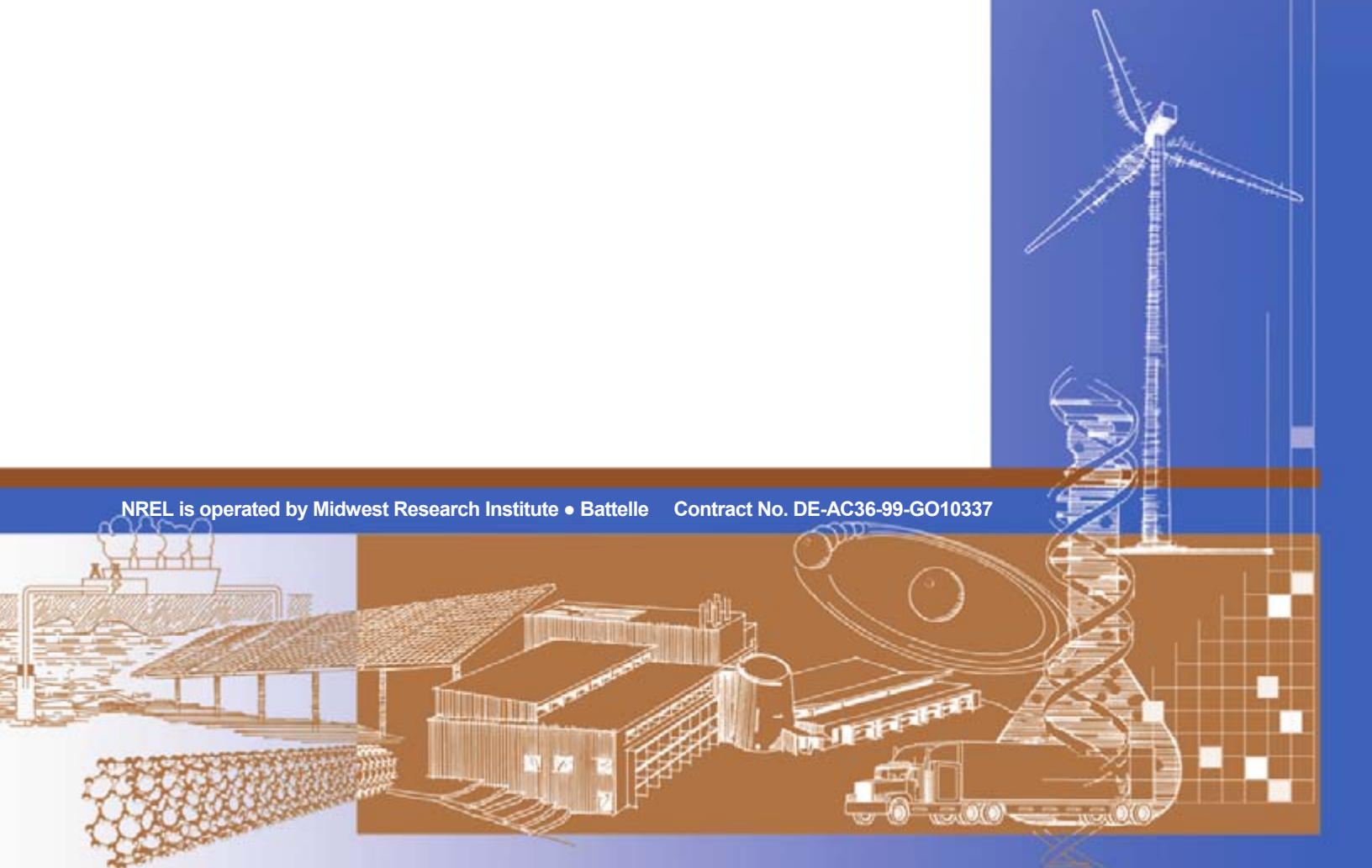

NREL is operated by Midwest Research Institute • Battelle Contract No. DE-AC36-99-GO10337

Lidar for Turbine Control

March 1, 2005 – November 30, 2005

M. Harris
QinetiQ Limited
Malvern, Worcestershire, United Kingdom

M. Hand, A. Wright
National Renewable Energy Laboratory
Golden, Colorado

NREL Technical Monitor: S. Schreck
Prepared under Task No. WER6.0301 and Subcontract No. YAM-5-33200-11

Technical Report
NREL/TP-500-39154
January 2006

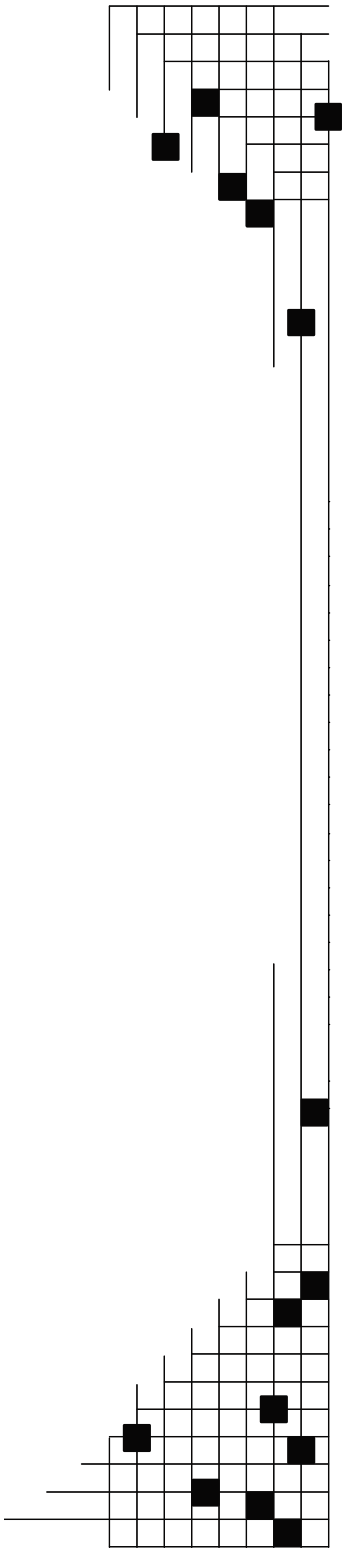

National Renewable Energy Laboratory
1617 Cole Boulevard, Golden, Colorado 80401-3393
303-275-3000 • www.nrel.gov

Operated for the U.S. Department of Energy
Office of Energy Efficiency and Renewable Energy
by Midwest Research Institute • Battelle

Contract No. DE-AC36-99-GO10337

Executive Summary

This work represents the first study (to our knowledge) that explores the potential of a turbine-mounted laser anemometer to enhance capabilities for wind energy production. The study combines laser anemometry (lidar) know-how from QinetiQ, Malvern, United Kingdom, with turbine design and control system expertise from the National Wind Technology Center (NWTC) at the National Renewable Energy Laboratory (NREL), Colorado, United States of America.

Lidar offers a method of remote wind speed measurement. The technique was first demonstrated in the 1970s and has been used in a number of research applications. Widespread deployment of the technique has so far been hampered by the expense and complexity of lidar systems. However, the recent development of lidar systems based on optical fiber and components from the telecommunications industry promises large improvements in cost, compactness, and reliability so that it becomes viable to consider the deployment of such systems on large wind turbines for the advance detection of fluctuations in the incoming wind field. Potential advantages of this approach include increased turbine energy output and reduced turbine fatigue damage (increased lifetime); here we only explore the latter.

The overall goal of the Lidar for Turbine Control study is to examine the requirements of a forward-looking lidar system, along with the associated interface to the turbine control systems. Different lidar options have been considered, including design choices such as output power, transceiver, signal processing, as well as turbine mounting and scanning options. Three configurations have been analyzed in more detail: Configuration #1 is the cheapest basic option, Configuration #2 is an intermediate option, while Configuration #3 has the greatest capability and cost. The lidar costs have been calculated on the basis of the production of 250 turbine-mounted lidar units per year with an initial run of 150 units. The final costings, which rely on assumptions and must be treated with caution, range from $45,000 to $95,000. Each of the options can accurately measure the axial component of wind speed in a timescale of order 10s of milliseconds. Hence, by scanning the beam it is possible to build a picture of the wind field in front of the turbine.

A generic method for analysis of lidar output has been examined, allowing a modelling representation of the lidar input to the control system. This involves derivation of the line-of-sight component of wind speed for each point interrogated, followed by a weighted summation of these components to derive the lidar spectrum for a given geometry. Full-field simulated turbulent wind fields are created using TurbSim, a code developed by NREL that generates a binary data file containing u, v, and w velocity components at evenly spaced grid points in a plane. A module was then added to the FAST aeroelastic wind turbine simulation code to simulate a lidar device. The current study explores the inclusion of forward-looking lidar as input to a control algorithm to mitigate fatigue loads at the blade root in above-rated wind speed conditions.

The use of forward-looking lidar could enhance a wide range of control systems in a number of regimes; however, the scope of this study is restricted to examination of speed regulation and load mitigation in Control Region 3 for the NWTC's CART (Controls Advanced Research Turbine). This is a 2-bladed, teetered-hub, variable-speed machine, but a rigid hub was simulated in this study. The turbine is rated at 600 kW; it has a 43-m rotor diameter and a 36-m hub height. At rated power, the turbine rotates at 41.7 rpm. It is outfitted with servo-electric motors capable of pitching the blades independently, precisely, and quickly. This wind turbine was selected for this simulation study because a number of sophisticated control algorithms have been tested on it. The results indicate that damage equivalent flap loads can be reduced by approximately 10% under turbulent wind inflow conditions when lidar signals are included as measurements to the controller. Studies such as this could eventually feed into an estimate of the reduction in cost of energy (COE) that would result from the widespread deployment of turbine-mounted lidar.

As a first study in the field of turbine-mounted lidar, this work has identified a number of potential areas for future research, including further modelling investigations to examine some of the other regimes identified. Controllers that include lidar-based wind measurement inputs must be specifically designed for each of the operating regimes. Eventually the modelling studies must extend to larger-scale turbines in order to arrive at a realistic estimate for the reduction in the COE. Current industry standard machines are rated at 1.5 MW with rotor diameters on the order of 80 m, but many companies are developing even larger turbines.

It would also be highly desirable to conduct experiments on turbine-mounted lidar to verify the results of the modelling work. Any scheme would ideally retain enough flexibility to explore different scan patterns and focus range options. These lidar experiments will also provide the capability for a wider range of investigations, including power curve measurement and turbine wake and shadowing studies. Also, field testing is required to address concerns regarding the true correlation between upwind flow measurements and the turbine response. These differences cannot be simulated with current simulation capabilities.

Table of Contents

1 Introduction

Laser anemometry (lidar) offers a method of remote wind speed measurement. The technique was first demonstrated in the 1970s and has been used in a number of research applications. Widespread deployment of the technique has so far been hampered by the expense and complexity of lidar systems. However, the recent development of lidar systems based on optical fiber and components from the telecommunications industry promises large improvements in cost, compactness, and reliability so that it becomes viable to consider the deployment of such systems on large wind turbines for the advance detection of fluctuations in the incoming wind field. Potential advantages of this approach include increased turbine energy output and reduced turbine fatigue damage (increased lifetime); we only explore the latter in the current report.

Established by the United States Department of Energy Wind Energy Program, the Low Wind Speed Technology (LWST) Project aims to develop technology that will enable wind systems to generate cost-competitive electrical energy at low wind speed sites. The sites targeted by this effort have annual average wind speeds of 5.8 m/s, measured at a 10-m height. Such sites are abundant in the United States and would increase the available land area that can be economically developed by twentyfold. The program goal is: By 2012, reduce the cost of electricity from large wind systems in Class 4 winds to 3.6 cents/kWh for onshore systems and by 2014, reduce the cost of electricity from large wind systems in Class 6 winds to 5 cents/kWh for shallow water (depths up to 30 meters) offshore systems.

The overall goal of the Lidar for Turbine Control study is to examine the requirements of a forward-looking lidar system, along with the associated interface to the turbine control systems. We consider different installation options and perform an analysis of the costs and benefits of achieving enhanced performance and reduced maintenance. The report provides a summary of the lidar technique (Section 2) and a review of the various available turbine-mounting options (Section 3). From the numerous possible combinations, we analyze three configurations in detail (Section 4) and estimate their costs and capabilities. Next we examine the analysis of lidar output, allowing a modelling representation of the lidar input to the control system (Section 5). The control studies in Sections 6 and 7 analyze and quantify the potential advantage of advanced wind speed warning via turbine-mounted lidar. These studies could eventually feed into an estimate of the reduction in cost of energy (COE) that would result from the widespread deployment of turbine-mounted lidar. Sections 8 and 9 summarize the overall conclusions and propose further stages of investigation.

2 Overview of Lidar Techniques

A number of optical and acoustic methods have been developed that allow measurement of fluid velocities; reference [1] provides a useful recent review of the range of available wind-sensing equipment. In this report, we concentrate on the technique of coherent laser radar (CLR), also referred to as lidar, ladar, and CDL (coherent Doppler lidar), for the remote measurement of wind speed in the atmosphere. Lidar involves the emission of a coherent light beam and detection of the weak return reflected or scattered from a distant target. The technique provides a means to measure the line-of-sight component of wind speed via detection of the Doppler shift for light backscattered from natural aerosols (particles of dust, pollen, droplets, etc.) in the atmosphere. A basic underlying assumption that the scatterers accurately follow the flow is usually very reliable except in precipitation. The principles of lidar are described in more detail in Section 2.1.

Other techniques for measurement of flow velocity include laser Doppler anemometry (LDA), also known as laser Doppler velocimetry (LDV), which detects the intensity modulation from particles traversing the fringe pattern created by the intersection of two laser beams [2], the modulation frequency being proportional to the transverse component of the particles' velocity. LDA is commonly used in wind tunnels but is inappropriate for atmospheric wind speed measurements: it lacks sensitivity at ranges beyond a few meters and seeding is normally required. The nomenclature requires care and can be misleading: CLR systems are sometimes described as "reference beam LDA."

Particle imaging velocimetry (PIV) is another powerful technique for flow measurement in wind tunnels [3]. Like LDA, it requires the flow to contain seeding particles and is therefore unsuitable for atmospheric measurements. The same comments apply to the technique of Doppler global velocimetry (DGV) [4].

Incoherent (or "direct detection") Doppler lidar is an alternative for atmospheric measurement of wind speed [5]; these pulsed systems usually operate in the UV and rely on molecular scattering to provide the return signal. While the capabilities of incoherent lidar are impressive (they are being considered for space-based global wind measurements), their current size, cost, and complexity suggest the technique is inappropriate for the turbine-mounted application considered here.

Sodar is a commonly used method of remote atmospheric wind profiling. It involves the emission of sound pulses and relies on the detection of the weak echo scattered from temperature and velocity fluctuations in the atmosphere [6]. It measures the wind velocity via the Doppler shift of the acoustic pulses in a manner analogous to lidar. It is unlikely that sodar will be suitable for the application examined in this report: the background acoustic noise in a turbine-mounted location is likely to disturb the measurement, and side lobes on the emitted sound beam will inevitably strike solid objects (blades, the ground, etc.) leading to spurious returns. In addition, the sensitivity is typically lower than for lidar leading to much reduced data rates.

2.1 Basic Principles of CLR

The principle by which coherent laser radar measures the velocity of a target is deceptively simple: a beam of coherent radiation illuminates the target, and a small fraction of the light is backscattered into a receiver. Motion of the target along the beam direction leads to a change $\delta\nu$ in the light's frequency via the Doppler shift, given by:

$$\left|\delta\nu\right| = \frac{2V_{LOS}}{c}\nu = \frac{2V_{LOS}}{\lambda} \tag{2.1}$$

where c is the speed of light (3×10^8 m s^{-1}), V_{LOS} is the component of target speed along the line of sight (i.e., the beam direction), and ν and λ are respectively the laser frequency and wavelength. This frequency shift is accurately measured by mixing the return signal with a portion of the original beam and picking up the beats on a photodetector at the difference frequency. The essential features are readily seen in the simplified generic CLR depicted in Figure 1. To illustrate the concept, this is drawn as a bistatic system in which the transmit and receive optics are separate and distinct. In practice, a monostatic geometry is more usual, in which the transmit and receive paths share common optics.

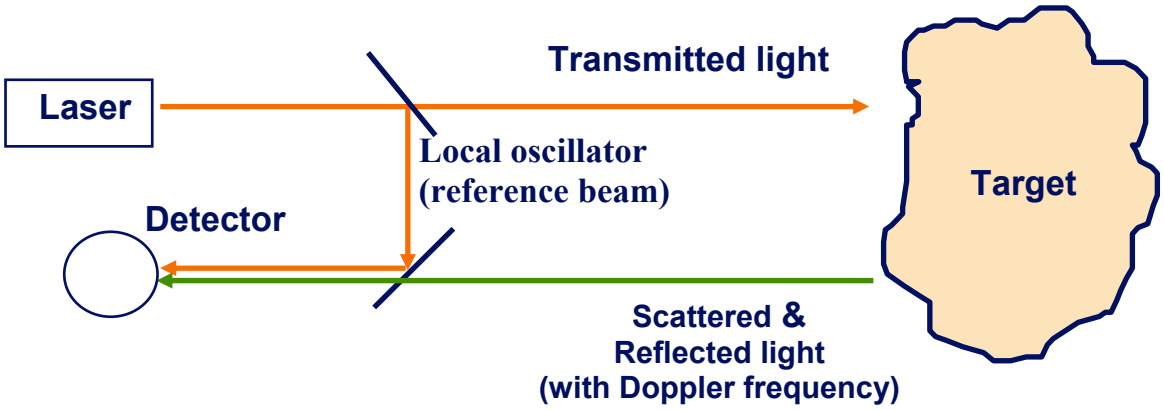

Figure 1. Generic coherent laser radar (CLR) system

The reference beam, or local oscillator (LO), plays a crucial role in the operation of a CLR. Firstly, it defines the region of space in which light must be scattered for detection of the beat signal; radiation from other sources (e.g., sunlight) is rejected, so CLR systems are usually completely immune to the effect of background light. The LO also provides a stable reference frequency to allow precise velocity determination; as a consequence, CLR systems are inherently calibrated, provided there are no gross drifts in laser frequency. Finally, the LO amplifies the signal via the beating process to allow operation at a sensitivity that approaches the shot-noise (or quantum) limit. This very high sensitivity permits the operation of CLR systems in an unseeded atmosphere, relying only on detection of weak backscattering from natural aerosols.

Figure 2 illustrates the stages of signal processing required for CLR wind signals. The detector output, containing the beat signal information embedded in broadband noise, is typically digitized by an analog-to-digital converter (ADC). Spectral analysis (e.g., by fast Fourier transform methods) leads to the generation of Doppler spectra. It is usually necessary to average a number of these spectra to improve the signal-to-noise ratio (SNR), after which the Doppler peak should stand clearly above a flat shot-noise floor. A value for the line-of-sight wind speed can then be computed via a velocity estimation algorithm. This might calculate, for example, the peak or centroid value of the Doppler peak.

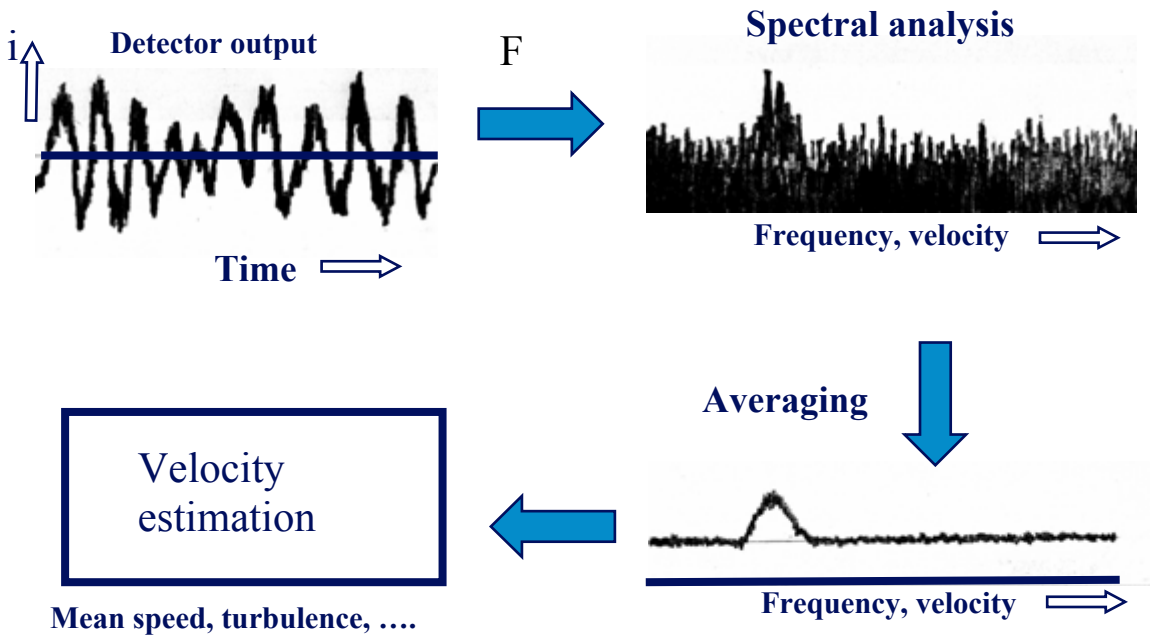

Figure 2. Outline of lidar wind signal processing

Lidar has been used in a wide range of atmospheric research applications:

- Wind profiling
- General meteorological investigations
- True airspeed measurement
- Characterization and tracking of aircraft wake vortices [7, 8]
- Monitoring of gaseous species (DIAL, or differential absorption lidar).

In addition, it has a number of applications related to the interrogation of hard targets:

- Rangefinding
- 3D imaging
- Remote vibration analysis.

2.2 Continuous Wave (CW) Lidar

CLR systems can be either of pulsed or CW type. In its simplest embodiment, the lidar emits a continuous unmodulated radiation beam. The detector output is then processed in discrete chunks at a rate determined by the signal processing and other system requirements. Such systems achieve operation at different ranges by focusing at each chosen range in turn. Focusing of the lidar beam results in a Lorentzian spatial weighting function centered on the beam waist. The half-width of this function is determined by the Rayleigh range (i.e., the distance from the waist at which the beam area has doubled its value at the waist), and this increases roughly as the square of the range. CW systems have an inherent maximum range (usually of order a few 100s of meters) beyond which it is impossible to focus the beam because of diffraction. A variant of CW lidar, frequency-modulated continuous wave (FMCW), has been used to

improve the range-resolution capability [9], but this is only effective with hard targets and is not an appropriate technique for wind speed measurement.

In wind speed measurements, the target scattering material is assumed distributed evenly throughout the probe volume. Under this condition, the time-averaged received optical signal power P_S is well approximated by [10]:

$$P_S \approx \pi P_T \beta(\pi) \lambda \tag{2.2}$$

Where P_T is the transmitted laser power, $\beta(\pi)$ is the backscatter coefficient in $(\text{m sr})^{-1}$, and λ is the laser wavelength. Hence CW CLR possesses the interesting property that the return signal power has no dependence on range or aperture size[1]. Taking a value of $\beta(\pi)$ for clear boundary-layer air of 10^{-8} $(\text{m sr})^{-1}$ for a wavelength 1.5μm, we obtain a value of $\sim 5 \times 10^{-14}$ for the fraction P_S/P_T of transmitted photons that are received by the system. This emphasizes the need for high sensitivity, with a received photon rate of $\sim 7 \times 10^5$ s^{-1} for 1W of emitted radiation.

2.3 Pulsed Lidar

In a pulsed lidar, the radiation is emitted in short bursts, typically of a few microseconds [11,12]. This approach allows range measurement from the time-of-flight and permits operation to much longer ranges (>10 km). Data from each range bin are obtained in parallel, in contrast to CW systems that must probe different ranges in series. The short pulse duration necessarily degrades velocity resolution, and there is a direct trade-off between range resolution (ΔR) and velocity resolution (ΔV_{LOS}). These are determined by the approximate relations below for a pulse length T:

$$\Delta R \sim \frac{T c}{2}; \qquad \Delta V_{LOS} \sim \frac{\lambda}{4\pi T} \tag{2.3}$$

As an example, a range resolution ΔR of 10m requires a pulse length T ~ 60ns, giving a velocity resolution $\Delta V_{LOS} \sim 2$ m s^{-1} for wavelength $\lambda = 1.55$μm. Note, however, that the mean value of V_{LOS} can be determined to much higher accuracy than ΔV_{LOS}.

2.4 Choice of Laser Wavelength

The best choice of wavelength for a lidar system depends on several factors, including eye safety, performance, and cost and availability of technology.

Eye safety is assumed to be a prerequisite for the application considered here. Although the risk of a turbine-mounted system illuminating maintenance personnel is small, the system must achieve laser Class 1 or 1M [13]. While it is possible to operate safely at a higher class rating, this will probably result in an unacceptable administrative burden involving, for example, the need to provide a trained Laser Safety Officer at each installation. Wavelengths longer than 1.4μm do not penetrate the eye and cannot reach the retina; hence a higher power emission is permitted within Class 1 at these wavelengths. With this restriction in mind, the available technology currently narrows the choice in practice to 3 three wavebands centered around 1.5μm, 2μm, and 10μm. The earliest lidar systems [14,15] used 10.6μm CO_2 gas laser sources, but these require cryogenically cooled detectors; large, expensive optical components; and

[1] A larger lens (or shorter range) subtends a greater solid angle at the target region, leading to the more efficient collection of light scattered from the probe volume. However, the probe volume becomes smaller, so it scatters less light in the first place. These two effects cancel, leading to the independence of signal on aperture and range until the maximum range is approached.

delicate, free-space alignment optics. We conclude that such systems are unsuitable for the current application. Solid-state 2μm systems have reached a high level of development but are probably more suitable for long-range pulsed applications. Optical-fiber-based 1.5μm systems have been developed to exploit recent advances in the telecommunications industry. The use of fiber greatly simplifies system alignment, and highly reliable components are generally available off-the-shelf.

The overall performance of a CW CLR wind sensor is not a sensitive function of its wavelength. While more light is scattered from aerosols at shorter wavelength, long wavelength systems are inherently more sensitive [16] (reasons include the emission of more photons per Watt of laser power and reduced Doppler shifts leading to lower noise bandwidth). These effects largely cancel, leaving an overall dependence in SNR of order $\lambda^{0.5}$ in the relevant weak signal regime of low $\beta(\pi)$. The slight advantage this confers on long-wavelength systems is more than offset by convenience and cost considerations: We conclude that fiber-based systems at 1.5μm are the best choice for this application. So far, only systems of this type have been successfully deployed for turbine-mounted lidar wind speed measurements (Section 3.1).

2.5 The QinetiQ ZephIR Lidar System

In the mid-1990s, the QinetiQ lidar team investigated alternatives to its existing CO_2 lidar systems. New developments in optical fiber and related components from the telecommunications industry offered a promising approach to lidar construction. The team successfully demonstrated CW all-fiber lidar anemometers (at a wavelength 1.55μm) in the late 1990s [9,16] and have remained at the forefront with the development of a commercial fiber lidar system (ZephIR) that has an established track record of successful wind measurement in a number of applications related to the wind power industry [17-21].

QinetiQ began a program to develop a commercial fiber-based laser anemometer in 2001. Progress has been rapid, building on previous fundamental work, and prototype systems have been deployed successfully in several demanding applications. Initial deployment of the ZephIR laser anemometer (March 2003) was on the nacelle of a large (2.3-MW) wind turbine (Figure 3a), measuring the wind speed up to 200 m in front of the blades. The lidar consisted of a rack unit containing a laser source, detector, and signal processing computer situated in the base of the tower, connected via more than 100 m of electrical and optical fiber cable to the transceiver head mounted on the top of the nacelle. The lidar system was installed in one afternoon and was fully operational soon after, allowing advance warning of oncoming gusts and providing valuable experience in practical deployment issues.

The system was returned to Malvern after several weeks of successful operation. It was then converted into a ground-based scanning unit for wind profiling (Figure 3b) and was first tested in December 2003. It has since been used in numerous campaigns in the United Kingdom, Europe, and other parts of the world. The experience gained through these trials has built confidence in the robustness and reliability of the ZephIR design (see Appendix B). In late 2004, work began on a production instrument (Figure 3c), designed to perform autonomous wind profiling measurements for site surveys at proposed wind farm sites. The design process has concentrated on providing a reliable compact system that requires minimal maintenance and no re-calibration. Much effort has also been devoted to minimizing power consumption and the ability to operate successfully in extreme conditions (e.g., low and high temperatures).

Figure 3. Stages of evolution of the ZephIR lidar. Figure 3a shows the lidar head mounted on the nacelle of a Nordex N-90 wind turbine. Figure 3b shows prototype ground-based wind profiler at Risø wind energy test site, Høvsøre, Denmark. Figure 3c shows the ZephIR production model deployed in the field

The scanning version of the ZephIR lidar instrument has been widely employed as a wind profiler, measuring wind speed and direction from a ground-based platform to altitudes up to 150 m. This was achieved by offsetting the beam at an angle of 30 degrees to the vertical and scanning in azimuth at a rate of 1 revolution per second. As the beam rotates, it intercepts the wind at different angles, thereby building up a map of wind speed around a disc of air [22]. In a uniform air flow, a plot of Doppler velocity (V_{LOS}) versus scan angle takes the form of a rectified sine wave, with the peak Doppler values corresponding to upwind and downwind measurements:

$$V_{LOS} = \left| a\ \cos(\phi - b) + c \right| \tag{2.4}$$

where ϕ is the scan azimuth angle. A non-linear least-squares fit is performed of this model to the data, from which the three best-fit parameters—a, b and c—are extracted. The wind data is then computed as follows:

$$Horizontal\ speed\ (u) = a / \sin 30°$$

$$Vertical\ speed\ (w) = c / \cos 30°$$

$$Bearing = b$$

A possible ambiguity of 180° in bearing is normally easily resolved with reference to a simple wind-vane reading. When displayed as a polar plot, the output gives rise to a figure-of-eight (Figure 4). Figure 5 shows a typical result (from [17]) in which the 10-minute averaged values of horizontal wind speed obtained by the lidar are compared with those from a mast-mounted cup anemometer. Such verification is an important step toward wider deployment of lidar in the wind energy industry.

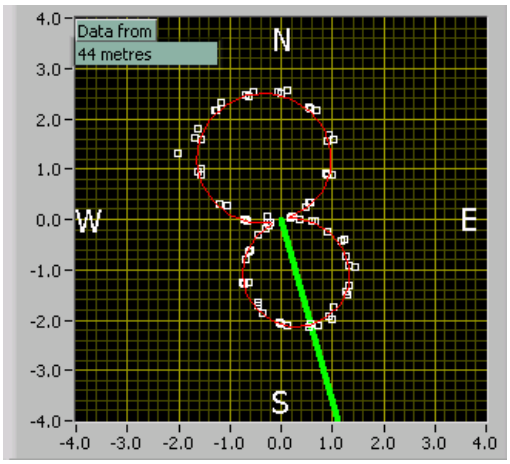

Figure 4. Polar plot of line-of-sight velocity component in m/s versus azimuth scan angle. White squares: 75 measurements obtained over 3 seconds. Continuous curve: best-fit solution. Bold line from origin: upwind bearing. The excellent fit indicates uniform flow across the scanned area. Note also a slight asymmetry in the lobe sizes, indicating a small vertical component to the wind velocity. By adjusting the focus, wind measurements can be made at all heights from 5 m to >150 m above ground level.

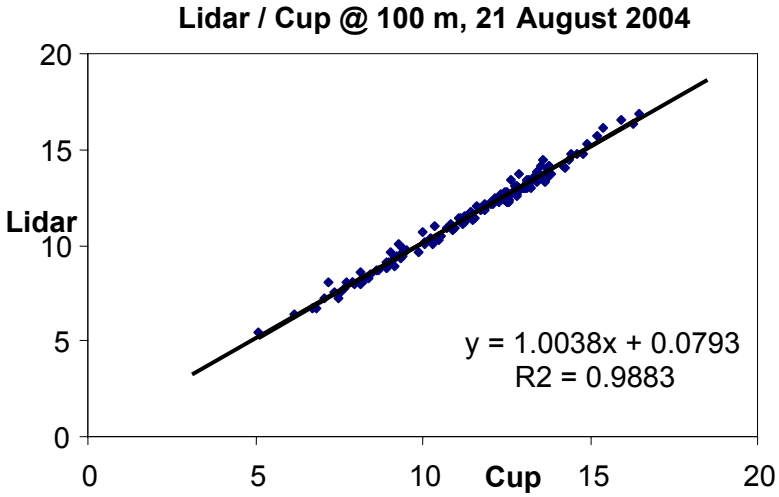

Figure 5. Regression plot of 10-minute averaged wind speed 100 m above ground in m/s, measured by lidar and calibrated cup anemometer. The lidar was situated 120 m from the base of the mast. The measurements were obtained over a 24-hour period when there was little risk of shadowing of the cup (by the mast or by adjacent turbines). The corresponding plots at other heights (40 m, 60 m, 80 m) display similarly good agreement and correlation.

The experience QinetiQ has gained with ZephIR and other related systems forms the basis for much of the detailed analysis of options presented in the following sections.

3 Options for Turbine-Mounted Lidar

3.1 Previous Work

While CO_2 coherent lidar has been used in some previous wind-power-related studies [23, 24], we are aware of only two examples in which lidar systems were mounted on a wind turbine. In the first experiment of this type to our knowledge, an early prototype of the QinetiQ ZephIR system was mounted on the nacelle of a Nordex N90 wind turbine at Postlow, 5 km west of Anklam in northeast Germany [20]. The lidar was configured as a continuous-wave (CW) monostatic design, capable of measuring line-of-sight wind speeds up to 39 m s^{-1}. The lidar transceiver was mounted on top of the nacelle (Figure 3a) and was connected by fiber optic and electrical cable to a control unit (in the base of the tower) containing the laser source, detector, and signal processing computer. The transmitted laser power would normally be ~1W; however, with the long (120 m) connecting fibers used here, the output was restricted to ~400 mW to avoid the non-linear optical mechanism of stimulated Brillouin scattering (SBS), which would lead to excessive noise and poor lidar performance.

The system stared straight ahead through the blades and could be focused at any range R from 10 m out to 200 m, and it was capable of measuring a value for wind speed approximately 10 times every second. Because the lidar beam was blocked approximately once per second by the rotating blades of the turbine, only 60% of measurements were successful, with the beam striking a blade in the remaining 40%. Such occurrences gave rise to very strong signals at low frequency (blade motion is nearly orthogonal to the lidar beam, so the Doppler shift is small) and are easily identified and rejected. The detector requires no recovery time from the intense blade reflection so that blocking presented no real problem in practice, with the lidar obtaining five or six independent wind measurements every second.

Data were acquired successfully over the full period of deployment, but to illustrate the lidar capability, we concentrate here on an 18-hour period when disturbance of the flow caused by adjacent turbines should be negligible. The wind speed data showed a striking increase in the turbulence level during this period, although the mean wind speed remained broadly similar throughout. During the evening (19:00-20:00), the airflow was remarkably stable and uniform; fluctuations increased through the night and became significantly more dramatic after sunrise (08:00 and later), exhibiting near-discontinuities in wind speed denoting the arrival of gusts, superimposed on a higher level of overall fluctuation. Figure 6 examines in more detail a good example of a gust, manifested as a sudden jump in speed at 08:44. In Figure 6b, the gust passes the beam focus at 200 m (corresponding to the midpoint of the lidar probe region) so that the two speeds contribute equally to the overall spectrum. The upper trace (Figure 6a), obtained 5 seconds earlier, is dominated by the lower speed, while 7 seconds later the lower trace (Figure 6c) shows virtually all the air in the probe volume moving at the higher velocity. The roughly 10-second timescale for the transition depicted in Figure 6 is consistent with the expected transit time of the gust through the lidar probe volume (~80m divided by 7 m s-1). There are many other gust events in the measurement sequence comparable to that displayed in Figure 6; however, a full and detailed interpretation of these events is difficult since the wind field is being probed only along a single line, and hence no information can be obtained on the transverse structure of the gusts.

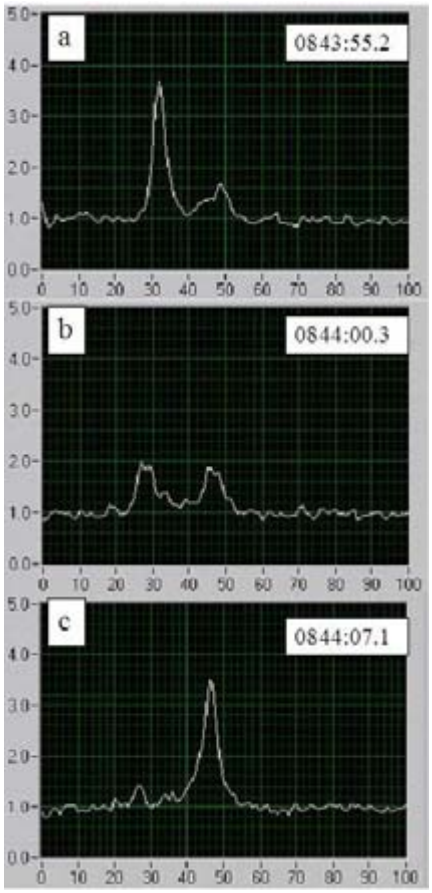

Figure 6. Evolution of Doppler spectra through a gust, with the time indicated on each plot. Plot (b) corresponds to a near-discontinuity in wind speed from 4 m s^{-1} to 7 m s^{-1}.

In another example of turbine-mounted lidar, a ZephIR system was installed by Risø on a test turbine for wake analysis. The lidar was mounted on a rearward-looking pan-and-tilt scanner, allowing measurement of wake wind speed deficit and wander [21].

3.2 Consideration of Turbine-Mounted Lidar Options

We begin with a summary of the generic characteristics that a lidar system must satisfy in this application. We envisage that the entire lidar will be mounted as an integrated unit, unlike previous turbine-mounted deployments discussed in Section 3.1. This will simplify installation and maintenance and eliminate any risk of problems due to SBS. The lidar must be eyesafe and achieve laser Class 1 or 1M. It must be capable of remote wind speed measurement at a rate of at least several Hz. The lidar must be economically viable over its entire lifetime, from initial procurement through ongoing in-service maintenance. And it must be capable of reliable operation in a wide range of environmental conditions. The specific lidar design options and requirements are now examined in more detail.

3.2.1 Environmental Conditions

The environment for either nacelle- or hub-mounted lidar is expected to be similar to that in an aircraft, with vibrations typically of order 0.5g at a few Hz. Neither mounting option results in a severe constraint on lidar size or shape. Temperature requirements are -40° C to +40° C. The lidar operating lifetime should be 20 to 30 years, with servicing at a minimum interval of 6 months, and a requirement for simple, rapid

removal. Other considerations include lightning surge protection; the effect of bugs, dust, and humidity on window transmission; and the possibility of damage from prolonged exposure to solar radiation.

3.2.2 CW Versus Pulsed Lidar

Pulsed lidar is a powerful technique for range-resolved measurement of atmospheric wind speed at considerable ranges of several km [11]. A pulsed lidar typically comprises the following elements: A stable master oscillator laser provides the coherent input to a pulsed optical amplifier, which then provides a train of transmitted output pulses. Care must be taken to maintain coherence during each pulse and avoid excessive frequency chirping. The local oscillator may be derived by tapping off a fraction of the master oscillator, and it is usually shifted in frequency to resolve directional ambiguity and avoid "wraparound" of the spectrum close to zero frequency. The target range is identified from accurate timing information requiring synchronization of the output pulse with the detection and signal processing electronics. By contrast, the elements of a CW system (laser output, detector, signal processing) operate entirely independently of each other and are possibly more compatible with modular construction. Parasitic scattering of the pulse within the transmitter can lead to saturation of the detection electronics for a finite time, leading to a minimum range that can be several tens of meters. This is avoided by a bistatic design at the cost of increased complexity (Section 3.2.5). The eye safety constraints (Section 3.2.3) can be more stringent for a pulsed system; however, for high pulse repetition rates, the Class 1 limit of mean power converges with that of a CW system. Care is also needed in optical-fiber-based pulsed systems to avoid non-linear optical effects such as SBS that can be generated by the high peak power of the pulse [12].

Overall we believe that it is currently not possible for a pulsed lidar design to satisfy all the requirements listed above, principally on the grounds of complexity, cost, and lifetime. In the discussion that follows it is therefore assumed that a CW system will be employed.

3.2.3 Output Power

The sensitivity of a CW CLR is directly proportional to its output power. High sensitivity is required to achieve a successful measurement rate in the clearest atmospheric conditions (i.e., when backscatter $\beta(\pi)$ is very low). As an example, the ZephIR production system emits $P_T = 1$W of laser radiation, giving rise to a minimum detectable backscatter of order $\beta(\pi) = 10^{-9}$ (m sr)$^{-1}$ for a 20 ms measurement time (50 Hz). For a reduced output of 200 mW, the minimum value of $\beta(\pi)$ required for wind speed measurement rises by a factor 5 to ~5 x 10^{-9} (m sr)$^{-1}$. This may result in a reduced level of availability, with the missed signal frequency possibly being a strong function of geographical location. Global atmospheric data on $\beta(\pi)$ at $\lambda = 1.5\mu$m is very sparse, so it is currently impossible to make reliable quantitative estimates of availability for a given system sensitivity. From experience (in England, Scotland, Denmark, Germany, and The Netherlands), $P_T = 200$ mW should provide availability >95% in Northern Europe[2] and other temperate maritime climates. The laser is the most expensive single component of the lidar, so there is a significant cost reduction associated with lower output power.

3.2.4 Transceiver Optics

The choice of lens aperture diameter has implications for system size/cost and performance. In general, the cost of a lens increases dramatically with its diameter. The resulting system is also likely to increase

[2] This estimate is based on the performance of the ZephIR prototype, which operated at $P_T = 1$W with reduced duty cycle and a sub-optimal detector. These amount to a deficit in sensitivity compared with the ZephIR production system of roughly a factor 5; hence the availability estimate is correct for an improved system with $P_T = 200$ mW.

significantly in weight and volume, and an increase in lens size does not improve sensitivity (Section 2.2). However, the lens size does impact on the maximum range and also on the probe volume (spatial resolution) for the wind speed measurement.

The lens quality must be high, with a need to achieve near-diffraction-limited performance[3]; a poor-quality lens will result in degraded spatial resolution. The issue of spatial resolution is analyzed in more detail in Section 5.1.2.

3.2.5 Monostatic Versus Bistatic

Bistatic CW lidar systems (with separate transmit and receive optics) are commonly used for hard-target applications such as vibrometry [25]. Bistatic CW wind lidars have also been successfully demonstrated [16] (Figure 7) and have the advantage of improved probe volume definition. In particular, the sensitivity weighting function cuts off rapidly, unlike the extended Lorentzian wings associated with a monostatic geometry (Section 5.1.2).

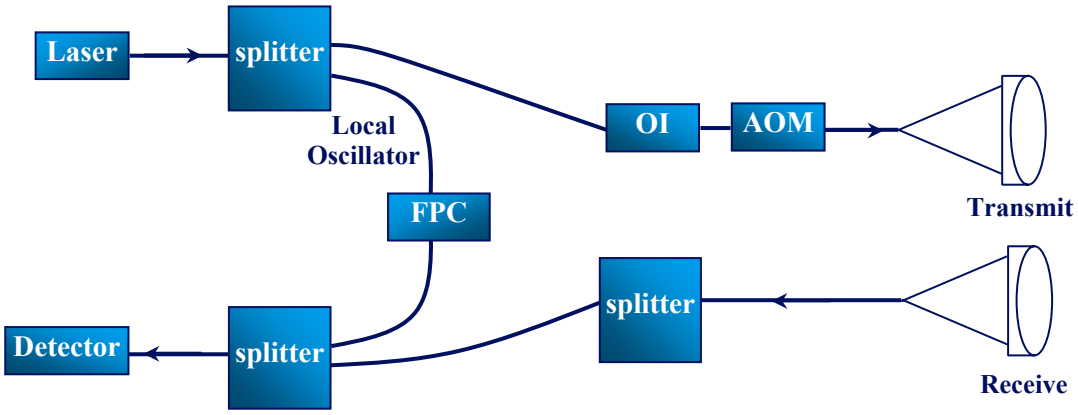

Figure 7. A simple all-fiber bistatic lidar design. Note the provision of an acousto-optic modulator (AOM) to allow direction sensing (Section 3.2.6)

However, a number of disadvantages associated with bistatic systems makes them inappropriate for this application. They are considerably more complex, requiring more optical components; a costly alignment and calibration process will likely be needed; they are prone to vibration; and they suffer a penalty in overall sensitivity. On this basis, we conclude that only monostatic designs should be considered further.

3.2.6 Direction Sensing

The local oscillator (LO) beam in a CLR is conventionally derived from a portion of the transmitted beam. Such systems are incapable of distinguishing the sign of the target motion (i.e., movement at the same speed, either toward or away from the lidar, leads to a signal at the same beat frequency). In order to build a lidar system that is capable of sensing the direction of motion, a difference in frequency must be created between the LO and transmitted beams. This is achieved by passing one of these beams through an acousto-optic modulator (Bragg cell), which imposes a frequency shift Δ (typically several 10s of

[3] The effect of lens quality on SNR can be quantified by considering the focused beam area in comparison with a diffraction-limited spot. The signal power from the target focal plane depends inversely on this area; if the focused spot has double the diffraction-limited area, then there will be a 3dB penalty for sensitivity in the focal plane.

MHz). Scattering from a stationary object then generates a beat at the "intermediate frequency" Δ, and the sign of any motion is derived according to whether the beat shifts up or down in frequency.

Again, the implementation of direction sensing comes with a penalty of increased complexity, reliability, and cost. A cost-benefit analysis must consider the likelihood of significant flow reversal in the forward-looking lidar geometry and also assess the possible penalty of being unable to distinguish such a flow reversal event. For wind profiling with the ground-based ZephIR system, directional ambiguity is usually resolved with a simple wind vane measurement; however, it is likely that this system will risk incorrect analysis of extreme flow reversal events.

3.2.7 Signal Processing

The optical beats that result from mixing the wind signal with the local oscillator are picked up on a photodetector. At a wavelength $\lambda \sim 1.5\mu m$, reliable InGaAs photodiodes are readily available that satisfy the essential requirements for a CLR of high quantum efficiency and low noise. The detector output must be spectrally analyzed in order to extract wind speed data; until recently, analog techniques such as surface acoustic wave (SAW) spectrum analyzers were common, but with current advances in computer power, digital methods are now becoming routine.

We illustrate the signal processing requirements with an example that is well matched to the needs of this application. An 8-bit ADC with a sampling rate of 100 MHz permits spectral analysis up to a maximum frequency of 50 MHz, corresponding to a wind speed V_{LOS} of 38.8 m s^{-1} (Eq. 2.1, with $\lambda = 1.55\mu m$). Spectra are calculated by digital Fourier transform (DFT) methods; a 512 point DFT will give rise to 256 points in the output spectrum with a bin width of ~200 kHz (corresponding to a velocity range of ~0.15 m s^{-1}). Each DFT will represent ~5μs of data; successive DFTs are then calculated, and the resulting power spectra are averaged to find a mean spectrum. The random fluctuation in the shot noise floor of the spectrum reduces as the square root of the number of averages; the sensitivity increases by this same factor. For 4,000 averages, the measurement time amounts to ~20 ms (or a data rate of 50 Hz). This assumes the processing is capable of 100% duty cycle, which has been shown to be achieved in ZephIR with a fast Fourier transform (FFT) block within a field-programmable gate array (FPGA), and it is likely that a standard fast PC with no additional duties to perform can achieve a similar performance. It is possible to accommodate reasonable variations in any of the above parameters (sample rate, DFT size, number of averages) and maintain the 100% duty cycle.

In conclusion, the choice of signal processing hardware does not impact greatly on the overall cost of the proposed lidar systems, and some flexibility on the choice of parameter values can be assumed.

3.2.8 Lidar Mounting

There are two main options for lidar mounting to consider: nacelle mounting and hub mounting. The relative merits are summarized in Table 1.

Table 1. Main Options for Lidar Mounting

	Pros	Cons
Nacelle mounting	Ease of mounting	Rotating blades block beam at ~1Hz
	Tested solution – low risk	Restricted field of view for some scan patterns
Hub mounting	Unobscured view	Installation more awkward
	Hub rotation can be used to provide conical scan without additional hardware by aligning beam at angle to rotation axis	Need to provide power to rotating hub and return wind speed data to nacelle

Overall the choice is between the greater simplicity of nacelle mounting and the improved capability associated with hub mounting.

3.2.9 Lidar Scanning

In general, the incoming wind field is turbulent, varying substantially in space and time and containing flow structures of different size and orientation. These fluctuations impose the fatigue loads that we seek to attenuate. The goal of scanning the lidar beam is therefore to provide a complete picture of the incoming wind field and hence provide the most beneficial input to the turbine control system to optimize performance. There are a wide variety of scanning options, to be considered here, ranging from a fixed focus, forward-staring arrangement to a fully programmable system that can interrogate any sequence of points in a 3D (x,y,z) scan pattern.

There are three options for lidar focusing (i.e., range adjustment), which are fixed focus, continuously variable, and limited number (e.g., three) of discrete range settings. In a fiber-based lidar, the focus is conveniently adjusted by moving the position of the output fiber relative to the focusing lens. A fixed focus system is simple, avoids moving parts, and involves low risk. The continuously variable option needs to maintain precise axial positioning of the fiber end (to within a few 10s of microns) and hence introduces lifetime and calibration issues. While the discrete setting option still contains moving parts, its performance is at lower risk of deterioration through years of operation.

Scanning options (Figure 8) include a conical scan, simply implemented with a rotating wedge as in the ground-based ZephIR system (as indicated above, this is available automatically for a hub-mounted system); linescan; and raster scan, which will require complex dual-prism or dual-mirror arrangement and is not considered further. Another interesting option that can provide a more complex scan pattern without excessive complexity is a combined hub/lidar conical scan, in which the lidar executes a conical scan that adds to that of the hub motion. Variation in scan pattern is possible by choosing the relative cone angles and scan rates for lidar and hub. In any scheme, the scan rate and cone angle must be chosen with consideration for area coverage and eye safety. A static focused 1-W 1.55μm beam will considerably exceed the maximum permissible exposure (MPE) of 1000 W m^{-2} (1 mW mm^{-2}), and such a beam can only comply with the laser Class 1 or 1M requirements if it is scanned so as to sufficiently reduce the mean, time-averaged, power at any given point in space. Continuous scanning is favored over a “scan, stop, and stare” scheme for this reason, and it is also easier to implement. Hence, there is a possible trade-off between cone angle, scan rate, lens diameter, and minimum range (large lens and short range resulting

in a tighter focus with shorter probe volume). However, in practice this does not impose a severe restriction, and the options proposed here fall well within Class 1M limits; in fact, a near-staring Class 1M option is possible at ranges beyond 20 m by introducing only a very small cone angle of 1 degree.

Figure 8. Examples of scanning options, showing hub-mounted staring scheme and hub-mounted conical scan

A number of other issues may influence the choice of scan pattern. Portions of a conical scan will clearly involve pointing the lidar beam with a downward or upward component, running a risk of striking the ground or clouds respectively. It is possible that these highly scattering objects, even though far from the beam focus, may provide more backscattered light than the actual wind signal of interest unless the lidar is of the more sophisticated pulsed or bistatic type. Returns from the ground are unlikely to cause a problem: stationary and slow-moving objects (<1 m s^{-1}) have only a small Doppler shift that can be simply eliminated via high-pass filtering (either pre- or post-spectral analysis). Returns from faster-moving objects such as cars will be clearly inconsistent with the overall wind behavior and can be addressed with outlier rejection algorithms. This also applies to spurious signals that can be generated when the lidar beam strikes birds or the moving blades of adjacent turbines. Scattering from clouds is a potentially greater problem, becoming more serious as the cone angle increases, as the range increases, and as the atmospheric backscatter reduces. Filtering algorithms have been developed at QinetiQ to eliminate cloud returns for the ZephIR wind profiler, and these could be further enhanced, if required, for use in this application.

Finally, the influence of rain on the measured wind speed must be considered; in rain, the falling drops provide a large fraction of the total backscatter, and there is a breakdown of the assumption that the scatterers faithfully follow the wind field. For a system in which the beam only points horizontally, errors from the raindrops' downward motion can be neglected, but wind speed may be slightly overestimated when the rain falls through a shear gradient and take some time to reach terminal horizontal velocity. Larger errors can occur when the beam has an upward- or downward-pointing component, as the drops' fall speed adds (or subtracts) from the true line-of-sight wind speed. The above effects are very dependent on droplet size, becoming more severe for large drops (e.g., a 0.2mm-diameter drop falls under gravity at speed ~1.2 m/s and reaches terminal velocity in a distance ~15 cm).

The overall decision on scanning is a choice between simple forward staring and more complex conical scan patterns that provide more information on the spatial wind field, but which may introduce errors in rainfall and spurious returns from clouds.

3.3 Summary

From the discussion in the previous section, we conclude it is likely that a cost-effective lidar system in this proposed application will be monostatic, continuous-wave, and at a wavelength of ~1.5μm allowing use of optical fiber and other telecoms components. Even with the rejection at this stage of certain options (bistatic, pulsed, etc.) and the concentration on fiber-based systems, there is still potentially a wide parameter space to examine, with consideration to be given to:

- Laser output power
- Aperture size
- Scanning options
- Mounting options
- Direction sensing.

The next section concentrates on three specific options with differing capabilities, allowing realistic estimates of the total system cost for each of the options.

4 Analysis of Chosen Configurations

This section describes the three chosen configuration options and their respective capabilities. The components of each system are identified, allowing an approximate cost breakdown. It is an assumption that all options must fall within laser Class 1 or 1M.

4.1 Summary of Chosen Options

4.1.1 Configuration #1

This is the cheapest basic option, comprising the following:

- Small aperture (diameter ~30 mm), monostatic, fixed focus (range ~50 m)
- No scanner, hub mounted for conical scanning
- Laser output power 200 mW.

The precise focus range is flexible and can be anywhere in the region of 20 m to 80 m with no impact on cost. The same comments apply to the choice of scanning cone angle. The lower laser power will result in reduced sensitivity and hence a possible reduction in wind speed availability.

4.1.2 Configuration #2

This is an intermediate cost option:

- Large aperture (diameter ~70 mm), monostatic, fixed focus
- No scanner, hub mounted for conical scanning
- Laser output power 1 W.

The larger aperture permits operation at longer range, with a maximum range on the order of 150 m (or possibly 200 m if the resulting extension of probe length is acceptable). The short range limit is of order 20 m; this value depends on the cone angle because of eye safety considerations. The 1-W laser power should ensure high availability with minimal drop-out rate.

4.1.3 Configuration #3

This option has the greatest capability and cost:

- Large aperture (diameter ~70 mm), monostatic
- Three discrete focus settings
- Laser output power 1W
- Conical scan
- Nacelle or hub mounted
- Direction sensing.

The system is capable of operation at long range and with high sensitivity. The focus settings can be at any range between 20 m and 200 m, and it will be possible to switch rapidly between them during operation. The conical scan will be achieved by a rotating wedge arrangement with a rotation rate in

the range of 0.3Hz to 3Hz; precise scan rate and cone angle have little impact on cost. The hub-mounted option will permit the most detailed spatial investigation of the incoming wind field with the potential to superimpose the lidar scan on the hub motion.

4.2 Comparison of Capabilities

Configurations #1 and #2 differ only in their sensitivity and spatial resolution. In the same conditions, #2 will achieve a SNR higher by a factor 5, and this will lead to a lower probability of "missed signals" and a higher availability. As previously discussed (Section 3.2.3), the improvement in availability is difficult to quantify, and it will vary with geographical location. The improved spatial resolution allows #2 to attain a greater potential maximum range, which is double that of #1. At a given range, the region of sensitivity (probe length) of #1 is roughly 4 times that of #2 (see Section 5.1.2 for quantitative analysis of probe length). Note that either #1 or #2 can be mounted on the nacelle for forward-staring operation, as long as a simple small-angle-wedge scanner is incorporated (a 1° cone angle is probably sufficient – Section 3.2.9) to satisfy eye safety limits.

Configuration #3 differs from the other two in its ability to scan and focus at different ranges. It also has the ability to measure the sign of the Doppler shift and distinguish flow reversals. Its sensitivity and availability will be the same as #2. It is at higher risk of disturbance from vibration, and it will require the use of more expensive polarization maintaining (PM) optical fiber and components, instead of the non-PM fiber of #1 and #2.

4.3 Analysis of System Costs

The following estimates of lidar costs have been calculated on the basis of the production of 250 turbine-mounted lidar units per year, with an initial run of 150 units. The estimate first takes into account component costs; these are generally available off-the-shelf from a range of suppliers, with the principal exception of the laser. The laser specification must satisfy stringent requirements for coherence length and intensity noise, and there are significant cost reductions through volume production. Despite this, the laser dominates the component cost in each of the three cases examined. Greater uncertainty is associated with the contributions to the cost from lidar assembly, calibration, and testing. In addition, we have taken into consideration the rough order-of-magnitude costs of installation, maintenance, warranty, and profit. The final prices, shown in the Table 2, must be treated with caution; they rely on certain assumptions and ignore likely future price variation.

Table 2. Lidar Costs

	Configuration #1	**Configuration #2**	**Configuration #3**
System price	$45,000	$60,000	$95,000
Includes laser cost	$10,500	$15,000	$20,000

In summary, Configuration #1 achieves a lower price than #2 by employing a lower-power laser and smaller optics. The higher price of Configuration #3 reflects the additional complexity associated with scanning, focus control, and direction sensing.

5 Lidar/Control System Interface

5.1 Algorithms to Derive Lidar Output from Synthesized Wind Field Data

In this section, we provide the means to derive the relevant simulated lidar data from a given realization of a synthesized wind field to provide input to the turbine control algorithms. The approach is not specific to a particular scan pattern. It is assumed that the wind field is described by values of the wind vector (u, v, w components – see Appendix A and Figure 9 for definitions) at discrete points forming a rectangular 3D grid (i.e., space is divided into a number of "boxes" and each wind vector represents some kind of average value for that particular box). A Cartesian coordinate system is assumed (see table of definitions) with the lidar located at (0,0,0).

There are three steps to derive the required lidar O/P at a given instantaneous value of scan angle:

1. Derive the component of wind speed along the beam direction ("line of sight") for each "box" intersected by the lidar beam.
2. Perform a weighted sum of these components to derive the lidar spectrum.
3. Use the spectrum to perform an estimation of line-of-sight velocity.

For Steps 1 and 2, it is a convenient approximation to ignore the motion of the beam during each individual measurement. Smearing over several boxes will only occur for scan patterns significantly faster than the current rate. In the prototype ZephIR system, the relevant timescale is 2.6 ms; in the upgraded production version with improved duty cycle, this increases to 20 ms. There is some flexibility in the choice of these values, involving a trade-off between SNR and measurement time ($SNR \propto \tau^{0.5}$).

5.1.1 Line-of-Sight Wind Component

Coherent lidar measures the Doppler shift resulting from the component of target velocity along the beam (or line-of-sight) direction. Motion of the target transverse to the beam direction produces no net Doppler shift. Hence, for a box located at (x,y,z) with wind components (u,v,w), the lidar will detect a line-of-sight velocity given by the dot product of the wind vector (u,v,w) and the unit vector along the beam direction:

$$V_{LOS} = \left| (u+v+w).\left(\frac{x+y+z}{\sqrt{x^2+y^2+z^2}} \right) \right| \tag{5.1}$$

Where the modulus implies a lack of direction sensing (i.e., the lidar is incapable of distinguishing motion toward/away). Eq. (5.1) simplifies to:

$$V_{LOS} = \left| \frac{ux+vy+wz}{\sqrt{x^2+y^2+z^2}} \right| \tag{5.2}$$

5.1.2 Weighting Function

The focusing of the lidar beam results in a spatial weighting function along the beam direction [10, 16]. (There is also a spatial dependence of sensitivity transverse to the beam, but because the beam is very narrow we can ignore it.) To simulate the observed lidar spectrum, we need to calculate the weighted sum of all the values of V_{LOS} for those boxes that the beam intersects.

To a good approximation, the weighting function for a continuous-wave (CW) monostatic coherent lidar (e.g., ZephIR) is given by a Lorentzian function:

$$F = \frac{\Gamma / \pi}{\Delta^2 + \Gamma^2}, \tag{5.3}$$

where Δ is the distance from the focus position along the beam direction, and Γ is the half-width of the weighting function (to -3dB point; i.e., 50% of peak sensitivity). Note that F is normalized such that its integral from $-\infty$ to ∞ gives unity[4]. To another good approximation, Γ is given by:

$$\Gamma = \frac{\lambda R^2}{\pi A^2}, \tag{5.4}$$

where λ is the laser wavelength (for ZephIR, 1.55×10^{-6} m), R is the distance of the beam focus from the lidar output lens, and A is the beam radius at the output lens (the beam intensity profile is assumed to be an axially symmetric 2D Gaussian; A is calculated for the point at which the intensity has dropped to $1/e^2$ of its value at the beam center). For example: in ZephIR, A takes the value 24 mm, so at a range R of 100 m, Γ has a value of ~8.5 m, or a probe length (to -3 dB points) of 2×8.5 m or ~17 m.

Further weighting may be performed to reflect the quantization of space. The contribution from each box should be weighted to reflect the beam/box interaction length (i.e., the length of the beam as it traverses each box).

5.1.3 Velocity Estimation

There are several options, but a calculation of centroid velocity (V_C) is a good first choice (this is the default method in ZephIR). These resulting values of V_C will provide the inputs to the control algorithm. In practice, with real lidar signals, the algorithm will be performed after a thresholding routine has been applied in order to discriminate the wind signal from the noise background. For this simulation, it is sensible initially to ignore noise and assume infinite lidar SNR.

Alternative approaches to centroiding include peak value V_P (the simplest option, though probably inappropriate in this instance where space is quantized) and median V_M (which is potentially more robust against spurious outliers).

5.2 Modelling of Wind Field and Derivation of Lidar Input

5.2.1 Simulated Wind Field

Full-field simulated turbulent wind fields are created using a code developed by NREL called TurbSim [26]. The TurbSim code generates a binary data file that contains u, v, and w velocity components at evenly spaced grid points in a plane. The grid size is generally chosen to encompass the wind turbine rotor with the maximum number of grid points. The number of grid points is limited

[4] The following are some quantitative examples to give a feel for the cut-off of the tails of the Lorentzian. Integration of Eq. 5.3 shows that 80% of the signal power originates from $\pm 3\Gamma$ of the focus, corresponding to the 10% points of the Lorentzian function. The 5% points correspond to $\pm 4.3\Gamma$, containing 86% of the signal power.

by computer memory capability. To simulate time-varying wind fields, multiple planes are created corresponding to a specified time step. This simulated turbulence is considered "frozen" in that the structures do not evolve over time. In the FAST aeroelastic wind turbine simulation code [27, 28], these planes "march" through the turbine rotor at the mean wind speed for the turbulence file. An illustration is shown in Figure 9. A subroutine in FAST computes the u, v, and w velocity components for a given (x, y, z) location by linearly interpolating between the grid points. This subroutine was used to obtain estimates of lidar measurements by providing a series of (x, y, z) points corresponding to points along the simulated lidar beam to obtain corresponding u, v, and w velocity components. The procedure outlined in Section 5.1 was then used to estimate the lidar output along the vector prescribed by the lidar beam.

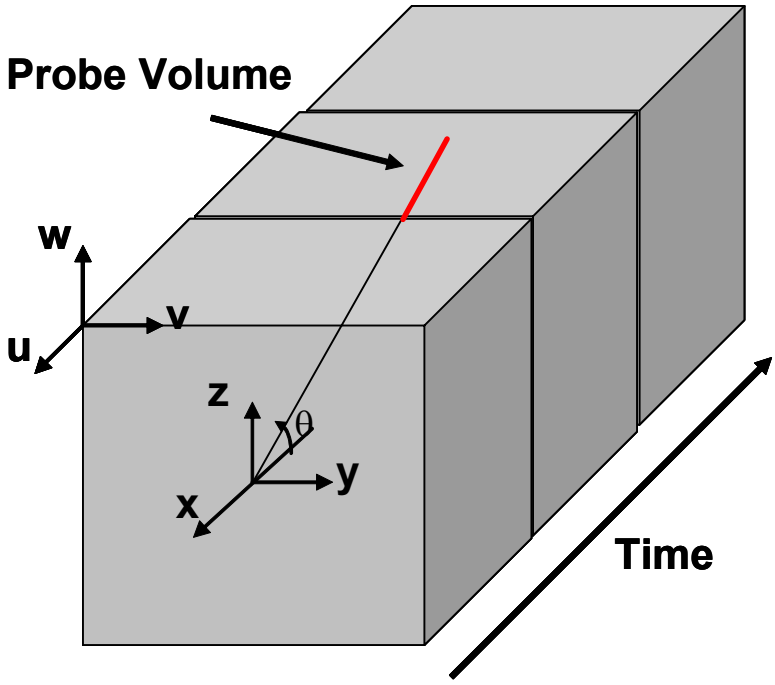

Figure 9. Illustration of marching planes representing turbulent flow field and lidar beam

5.2.2 Simulated Lidar Signal

A module was added to the FAST code to simulate a lidar device. To reduce necessary code modification, the lidar device is not attached to the turbine in any way. For instance, if the turbine should yaw with a wind direction change, the simulated lidar device will remain at its specified location and will continue to point along its specified vector. The lidar device cannot scan the flow field, but the number of devices that can be simulated is unlimited. For instance, a conical scan pattern can be defined by 36 individual lidar devices positioned as a common off-axis angle and spaced at 10° azimuth increments. Each simulated lidar device produces a velocity measurement at each simulation time step, and this is included with standard simulation output such as the blade azimuth angle and blade-bending moments. Subsequent manipulation of the multiple lidar outputs is required to simulate a single, hub-mounted lidar device that rotates with one of the turbine blades.

Figure 9 illustrates a lidar device located at the origin of the ground coordinate system. The origin occurs at the intersection of the turbine low-speed shaft with the center of the tower. The user must specify the Cartesian coordinates of the device, the off-axis angle (θ), and the azimuth angle that

define the vector along which the lidar points. In the example shown in Figure 9, the azimuth angle is 0° (which corresponds to the blade 1 azimuth angle convention). The user also specifies the focal distance, the lidar wavelength, and the beam radius. User-specified parameters specific to the mathematical modeling include the tail cutoff percentage and the number of points describing the weighting function. The procedure outlined in Section 5.1 is used to determine the line-of-sight velocity along the prescribed vector to simulate lidar output at every simulation time step.

In this study, the focal distance was selected to be 1 turbine rotor diameter (1D) to avoid complications with induced flow near the rotor. The lidar wavelength was 1.55e-6 m, and the beam radius was 0.024 m. A tail cutoff of 1% was chosen to capture the majority of the probe volume. One consideration for this parameter is that the simulated flow field is finite in the plane of the rotor; i.e., the grid of simulated turbulent wind has precisely defined y- and z-axes. The tail cutoff percentage specifies the distance from the focal point that is used to simulate velocity measurements along the Lorentzian function in Eq. 5.3. The grid size must be selected to accommodate the probe volume that extends from the focal point to the position defined by the tail cutoff percentage. As the focal distance increases, the defined volume also increases. Extending the wind field grid significantly beyond the turbine rotor diameter reduces the resolution of wind inputs to the aerodynamic model of the wind turbine simulation. The grid chosen for this study was 13 x 13, representing a square with 44-m sides. Thirty-one weighted velocity measurement points were used to describe the Lorentzian function defined in Eq. 5.3. Increasing the number of averaging points beyond 31 did not significantly alter the statistics. It appears that the Lorentzian function is adequately represented by 31 evenly spaced points.

The lidar configuration defined for the study consisted of a single, hub-mounted device that was focused in front of one of the turbine blades by canting the lidar device to some constant off-axis angle. A conical scan ahead of the turbine rotor would be achieved through rotor rotation. The off-axis angle, θ, was determined by positioning the lidar such that the focal point of 1D corresponded to a height above the hub center of 75% of the turbine radius, or 1D * sin (θ). Thus the lidar would obtain the wind velocities along a ring with a radius of 75% of the turbine radius upwind of the turbine, a distance of 1D * cos (θ).

To simulate this lidar configuration with the capability added to the FAST code, 36 simulated lidar devices were located in the wind turbine hub. They each pointed upwind of the rotor with an off-axis angle such that the 1D focal distance corresponded to 75% of the turbine blade radius. They were spaced at 10-degree azimuth increments. Thus, these 36 lidar devices observed wind speed corresponding to a ring with a radius of 75% of the rotor radius. A line-of-sight velocity measurement at each time step was output for all 36 lidar devices.

To simulate the single lidar device rotating with a turbine blade, subsequent processing of the 36 velocity measurements was performed. Based on the turbine blade azimuth position, the interpolated velocity between the two nearest lidar devices was computed. A moving average of velocity measurements over one complete rotor rotation was updated with each time step to provide an estimated uniform velocity over the rotor.

An estimate of vertical shear was obtained by subtracting the velocity as the rotor passed 180 degrees azimuth from the velocity as the rotor passed 0 degrees azimuth. This estimate of vertical shear was updated with each half of a rotor revolution.

Within a simulated wind field, the total velocity at four points representing azimuth positions of 0°, 90°, 180°, and 270° were averaged together at each simulation time step to create the “actual” disk average wind speed. This “actual” disk-average wind speed is compared to the lidar-derived moving azimuth average in Figure 10. Note that the lidar-based signal is derived upwind of the wind turbine disk. This distance produces a time shift of 2.1977 s for a mean wind speed of 18 m/s. Because the

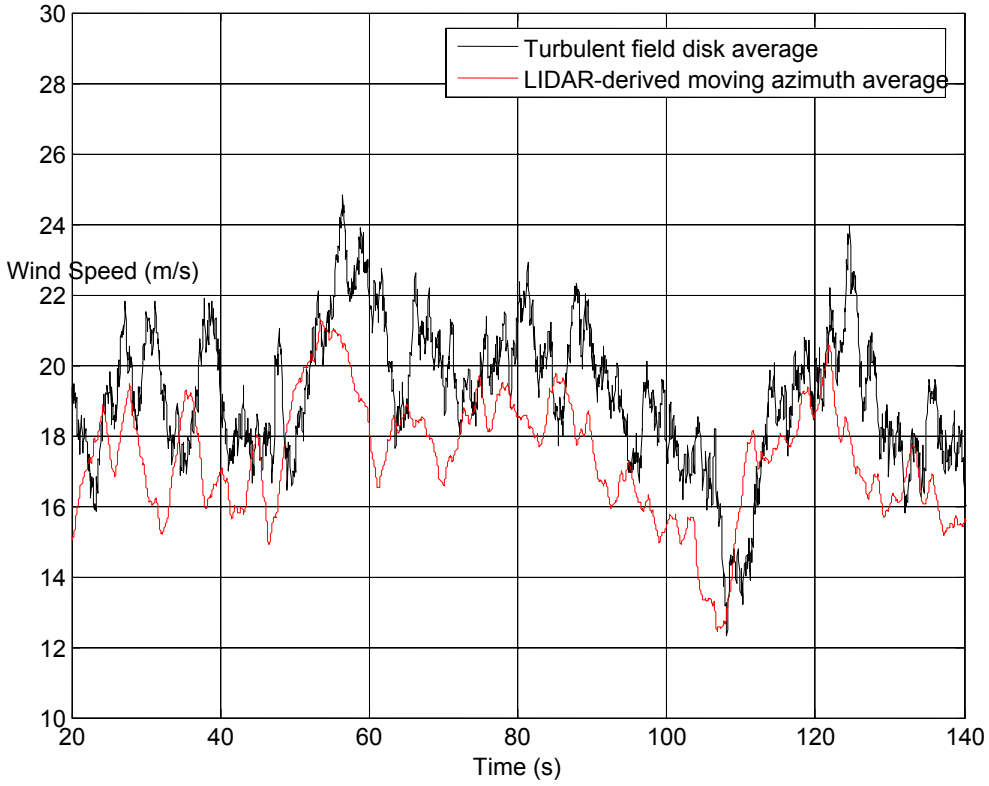

Figure 10. Comparison of actual turbulent flow field disk average and lidar-derived moving azimuth average wind speed

lidar observes line-of-sight velocity and is canted by the off-axis angle θ, it tends to underestimate the total velocity vector at the focal point. The moving average derived from lidar output does not retain some of the high frequency wind fluctuation, but the general trends are captured.

A comparison of the linear vertical shear across the rotor at each time step to the lidar-derived vertical shear is shown in Figure 11. The lidar-derived shear signal appears as a step function because the value at the top of the bottom of the rotor is updated every one-half rotor revolution. The time shift between the lidar measurement and the actual shear is evident in this figure.

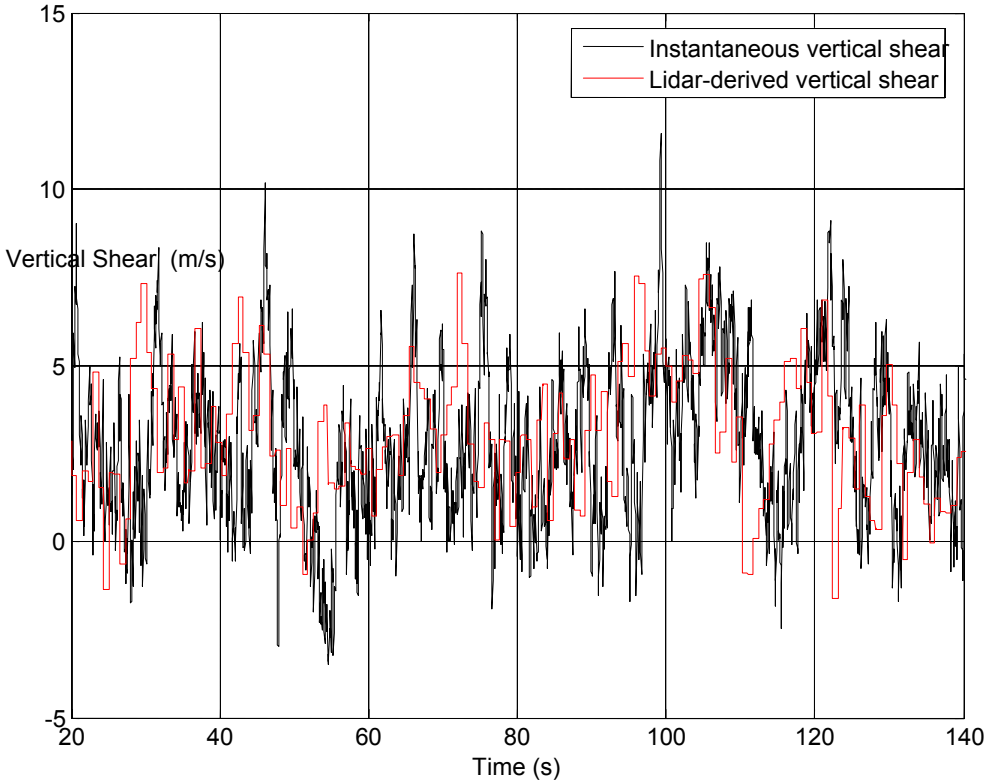

Figure 11. Comparison of actual turbulent flow field vertical shear across rotor and lidar-derived vertical shear

Several considerations are unique to the simulation environment and could not be duplicated in the real environment. For instance, the simulated turbulence upwind of the turbine is exactly the wind that impinges upon the rotor. In the real atmosphere, the wind is constantly evolving such that measurements upwind of a turbine are never perfectly correlated with the wind that actually impinges upon the turbine rotor. Analysis of experimental data from the LIST experiment conducted at the NWTC [29] showed that correlation coefficients between disk-averaged anemometers and wind turbine response over a distance of 86 m ranged between 0.92 and 0.94. The correlation was dependent on wind speed and data sample time. These data, sampled at 1 Hz, indicate that the correlation between upwind measurements and turbine response can be quite good.

6 Control Model: Assumptions and Objectives

6.1 Approach

To begin exploring the potential implications of including upwind wind speed measurements in sophisticated wind turbine control algorithms, this control simulation study was designed. The wind turbine was simulated using the FAST code [27, 28] developed by NREL. Another NREL code called TurbSim [26] was used to generate turbulent flow fields input to the wind turbine simulation. The wind turbine selected for this study was the Controls Advanced Research Turbine (CART) located at the NWTC. This turbine has been used for testing of sophisticated control algorithms.

Multiple wind turbine control systems are employed for several different turbine operating regimes. These control algorithms can improve energy capture and reduce dynamic loads during normal operation. Supervisory control algorithms start the turbine as the wind speeds increase and shut the turbine down when the wind speed exceeds the design criteria. Wind farm supervisory control algorithms maximize energy capture over multiple turbines. Use of forward-looking lidar could enhance each of these different control systems, as described in The scope of this study was restricted to one particular case, and this has been highlighted in boldface type in Figure 12.

I. Normal turbine Operation
   a. Region 2
      i. Energy capture improvements
         1. Assess possible improvements to current generator torque controls for optimum Cp tracking through input of Lidar measured wind disturbances
      ii. Load mitigation
         1. Assess improvements in load mitigation control schemes from input of symmetric and asymmetric wind disturbances. Assess reductions in rotor drive-train and tower loads.
   b. Region 3
      i. Speed regulation
         1. Assess improvements to speed regulation control through input of Lidar measured wind
      ii. Load mitigation
         1. Assess improvements in load mitigation control schemes from input of symmetric and asymmetric wind disturbances. Assess reductions in rotor drive-train and tower loads.
   c. Region 2 to 3 transition
      i. Assess potential of Lidar measured wind inputs to facilitate controller transitioning between regions 2 and 3.

II. Turbine Supervisory Control
   a. Startup
      i. Assess use of Lidar in measuring upwind windspeed to facilitate preparation of turbine for startup.
   b. Shutdown
      i. Assess potential of Lidar to measure high windspeeds and prepare turbine for shutdown before turbine experiences destructive loads.

III. Parked Turbine loads
      i. Assess potential of Lidar to measure extreme winds at a sufficient distance upwind of turbine so that turbine can be prepared (rotor re-positioned or nacelle yaw controlled) to minimize turbine loads during high wind events.

IV. Wind Farm Supervisory Control
   a. Explore use of Lidar to facilitate wind farm control.

Figure 12. Wind turbine control regimes that could be enhanced through the inclusion of forward-looking Lidar in control algorithms

In normal turbine operation, there are two distinct operational regimes. In below-rated wind speed conditions (Region 2), generator torque is commanded such that the wind turbine operates at variable rotational speeds to maximize energy capture. In above-rated wind speeds (Region 3), the blade pitch angle is controlled to maintain the rotational speed at a constant value such that the turbine produces power at the generator's rated level. Achieving a seamless transition between these two operational regimes (Region 2.5) creates additional control challenges.

Wind turbine designers simulate operation in normal turbulent flow fields as well as discrete, extreme events. Designs are driven by the maximum loads obtained through simulation of extreme

gusts and extreme wind direction changes and fatigue loads that contribute to lifetime damage calculations. As wind turbines become larger, either of these load types can become design drivers [30]. This study focused on the case in which the wind turbine operates normally in a turbulent flow field with the objective of reducing the fatigue loads. Mitigating fatigue loads reduces the corresponding damage, which ultimately leads to increased component life. This is one consideration in wind turbine design that may lead to reductions in cost of energy, and this operating condition was selected for further exploration in this study.

The current study explores the inclusion of forward-looking lidar as input to a control algorithm to mitigate fatigue loads at the blade root in above-rated wind speed conditions. Blade root-bending moments are generally computed about two orthogonal axes. The flap-bending moment results from the force applied in the predominant wind direction. The edge-bending moment is dominated by the gravity force as the blade rotates. Reduction of the flap-bending moment fatigue loads is the load mitigation objective for this study.

The damage equivalent load (DEL) parameter (F_e) is currently the wind industry's primary measure for quantifying these amplitude variations observed over some time period in relation to the fatigue damage attributed to the fluctuations [31-34]. Essentially, the equivalent fatigue load weights each cyclic variation of the load over the record using Miner's Rule, as shown in Eq. 6.1. The DEL represents a constant-amplitude, sinusoidal load applied at a constant rate over some period that would cause fatigue damage equivalent to that sustained by the fluctuating load amplitudes that result from the wind over the same period. In this study, a rain-flow cycle counting routine [35] was used to count full and half cycles.

$$F_e = \left[\frac{\sum_i (F_i)^m n_i}{N_o} \right]^{\frac{1}{m}} \tag{6.1}$$

In above-rated wind speeds, the primary control objective is to produce rated power by regulating blade pitch angles to maintain a constant rotor speed. Controller performance is generally assessed by minimizing the Root Mean Square (RMS) of speed deviation from the desired rotor speed and minimizing the peak speed deviation from the desired rotor speed. This study includes the objective of reducing the blade root flap DEL, the peak root flap-bending moment, and the range of flap-bending moments. Reducing these parameters indicates reduction in fatigue damage, which can extend the blade life. This simulation study explores this particular operating condition to assess the potential for inclusion of forward-looking lidar to improve control algorithms. Two types of controllers are compared, a typical Disturbance Accommodating Controller (DAC) and a DAC modified to include wind speed inputs obtained using lidar.

6.2 Wind Turbine Simulation

The wind turbine simulation was performed using FAST [27, 28]. This code uses aerodynamics subroutines included in AeroDyn [36, 37]. Although FAST is capable of simulating many degrees of freedom, this study modelled only the first blade flap-bending degree of freedom and the generator degree of freedom to simplify the controller design.

The wind turbine selected for modelling is the Controls Advanced Research Turbine (CART) located at NREL's National Wind Technology Center (NWTC) near Boulder, Colorado, USA [38-40]. This wind turbine is a two-bladed, teetered-hub, variable-speed machine, but a rigid hub was simulated in this study. The turbine is rated at 600 kW; it has a 43-m rotor diameter and a 36-m hub height. At rated power, the turbine rotates at 41.7 rpm. It is outfitted with servo-electric motors capable of

pitching the blades independently, precisely, and quickly. This wind turbine was selected for this simulation study because a number of sophisticated control algorithms have been tested on it [41-44].

Typical wind turbine controllers rely on single-input-single-output systems and are generally Proportional-Integral (PI) based controllers. These controllers have a single objective: speed regulation. Advanced controllers based on linear state-space models, such as DAC, are capable of achieving multiple objectives. These controllers regulate speed as well as mitigate wind turbine loads. Field tests at the NWTC on the CART have provided preliminary results that demonstrate the effectiveness of DAC compared to PI controllers [41, 44] in mitigating wind turbine loads, as well as regulating speed.

6.3 Wind Turbine Controller Designs

Sophisticated multiple-input-multiple-output (MIMO) control algorithms have been developed by NREL for wind turbine applications, primarily based on DAC theory [45-51]. These algorithms use linear, state-space representations of the wind turbine with state estimation. The wind input is considered a persistent disturbance that can be theoretically accommodated using a disturbance estimator [52]. These controllers require measurements of turbine response, such as the generator speed and tip deflection of each blade. In addition to these multiple inputs, multiple outputs, such as individual blade pitch angles, result. Individual blade pitch permits the alleviation of asymmetric blade loading that occurs when the mean wind profile presents a vertical shear across the entire rotor. For the purposes of this study, the DAC included five turbine states: rotor speed, Blade 1 tip displacement, Blade 2 tip displacement, Blade 1 tip velocity, and Blade 2 tip velocity. The wind disturbance was represented by three states: one for the uniform wind disturbance and two for the vertical shear disturbance. The DAC assumed measured inputs of the generator speed and the tip displacement of both blades. A diagram of the DAC simulation is shown in Figure 13. In addition to speed regulation, this controller is designed to reduce the blade load fluctuations that are induced by vertical shear across the rotor.

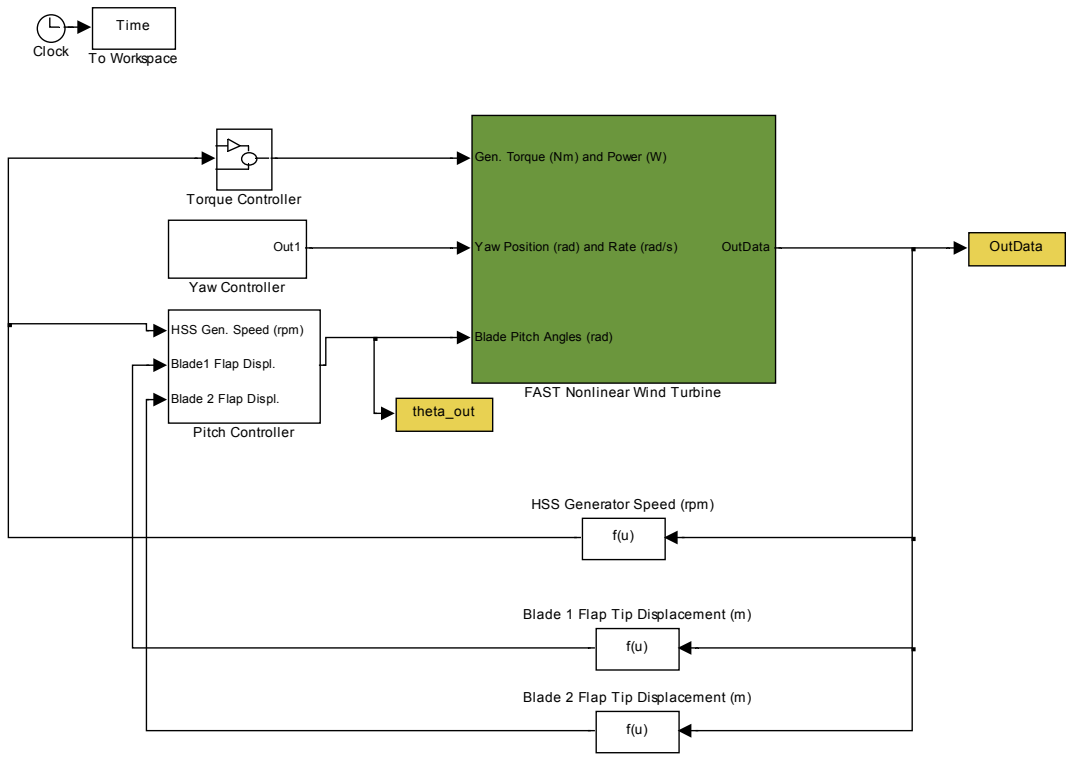

Figure 13. Diagram of wind turbine simulation with DAC controller

The controller that includes wind speed information obtained from the lidar (DAC + LIDAR) is based on a subset of states contained in the DAC controller. In the DAC + LIDAR controller, the shear disturbance is measured instead of estimated (as in the DAC controller). This eliminates the need to estimate two of the eight states (the original DAC controller estimated eight states). The remaining six states are estimated in the control model: generator speed, Blades 1 and 2 flap displacement and velocity, as well as the uniform wind disturbance. Measurements of the vertical shear across the rotor as a function of blade azimuth position are provided to the controller. A big advantage of the DAC + LIDAR controller is that blade-tip flap deflection measurements are no longer needed (as in the DAC controller).

Individual blade pitch angles are output. This controller must regulate rotor speed as well as mitigate blade load fluctuations related to vertical shear across the rotor. Figure 14 illustrates this controller. The simulated lidar measurement consists of the 36 individual measurements at 10° azimuth increments. The LIDAR box in the lower, left side of the figure contains the scripts that convert these 36 measurements into the difference between velocity at the top and bottom of the rotor plane (the azimuth average mean velocity is also computed, but it was not necessary for input to this controller). This shear value is then multiplied by the cosine of the azimuth angle to obtain the velocity fluctuation as a function of azimuth position.

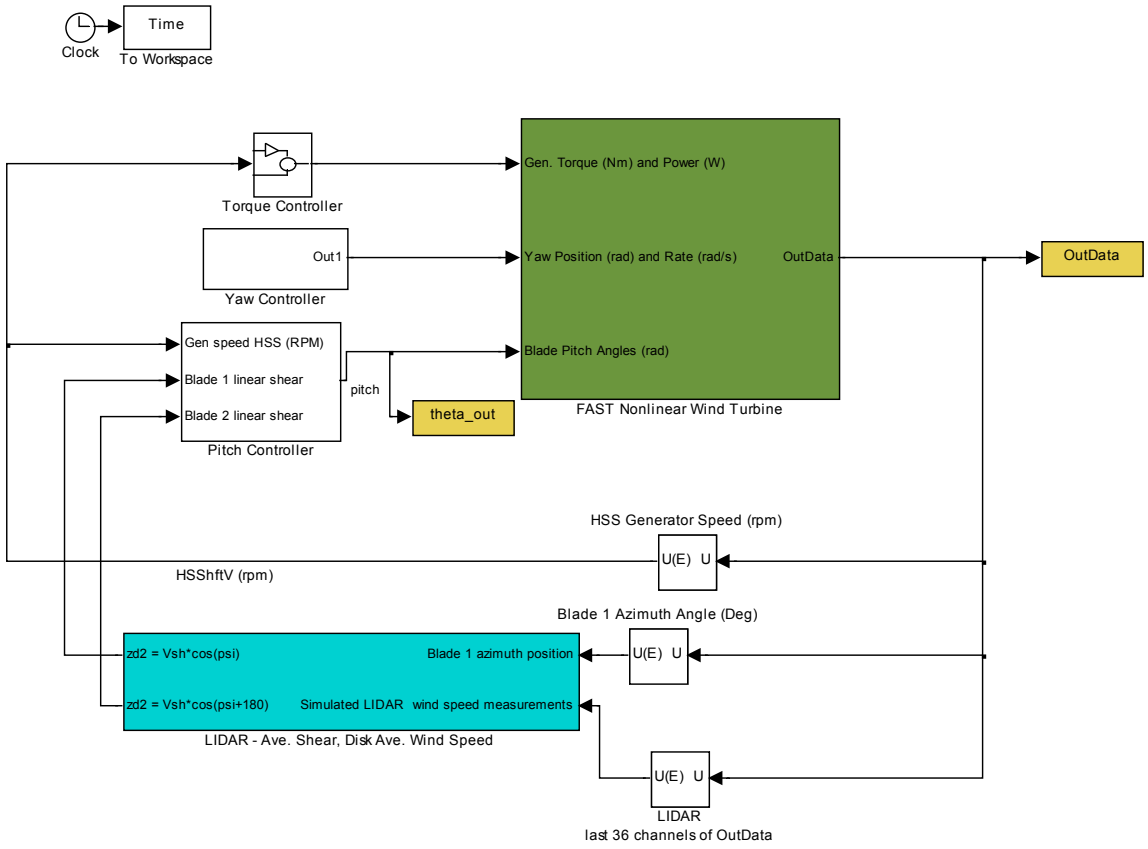

Figure 14. Diagram of wind turbine simulation with DAC+LIDAR controller

Four simulated wind conditions were selected to input to both of the controller models. Two steady wind conditions with power law exponents of 0.17 and 0.3 were simulated. Vertical shear as a function of height above ground is described with the following equation, where *m* represents the power law exponent:

$$W(z_g) = W * \left(1 + \frac{z_g}{h}\right)^m \tag{6.2}$$

These values were chosen because according to experimental data obtained at a site near Lamar, Colorado, 5-minute average shear exponents of 0.17 and 0.3 were observed 600 hours and 400 hours, respectively, during a 1-year period [53]. These are representative of average shear exponent values that a wind turbine would typically endure. These cases were 40 s in duration, but the first 20 s were neglected to exclude model startup transients. These cases show the idealized performance of both controllers.

Two turbulent wind conditions with similar power law exponents were also simulated to provide a more representative comparison among the different control algorithms. The turbulent wind cases are each 140 s in duration, and again the first 20 s are excluded to avoid startup transients. The lidar signals are delayed by 2.1977 s to accommodate the distance from the lidar focal distance to the wind turbine (42.672 m * cos(22.024°)), assuming a mean wind speed of 18 m/s.

7 Control System Study: Results and Analysis

7.1 Results

Simulations were performed for both of the controllers with each of the four wind fields described above. Table 3 summarizes the results of these simulations for the two steady wind conditions. The performance metrics related to speed regulation are the RMS of the speed error, or deviation from the desired rotor speed, and the peak speed error as a percentage of rated speed. For the steady wind conditions, these metrics are similar for both controllers, suggesting that the primary objective of speed regulation is achieved. The two controllers produce similar blade flap-bending moment response for the low shear case, but the DAC + LIDAR controller reduced the blade flap-bending moment response in the high shear case.

Table 3. Simulation Results for Steady Wind Conditions

	Steady 18 m/s wind, power law exponent = 0.17		Steady 18 m/s wind, power law exponent = 0.3	
	DAC	DAC + LIDAR	DAC	DAC + LIDAR
RMS speed error (rpm)	1.5	1.5	1.9	2.2
Max speed error (% of rated)	0	0	0	0
Blade 1 root flap bending moment DEL (kNm)	53	51	83	64
Blade 1 peak root flap bending moment (kNm)	304	297	317	301
Blade 1 root flap bending moment range (kNm)	59	58	93	72

The corresponding time series signals of the flap-bending moment, tip deflection, pitch angle, and rotor speed are illustrated in Figure 15 and Figure 16. The DAC and DAC + LIDAR controllers command a sinusoidal pitch angle variation to mitigate the load variation that results from sheared flow. The bending moment and tip deflection signals are comparable. The rotor speed is maintained at the desired speed of 41.7 rpm. For this steady wind condition, the amplitude of bending moment fluctuations is consistent. Because the range resulting from the DAC + LIDAR controller is less than that resulting from the DAC controller, the DEL is also reduced. In general, it appears that the inclusion of the wind shear measurement gives the controller more authority over load reduction as shear increases than inclusion of an estimation of the wind shear.

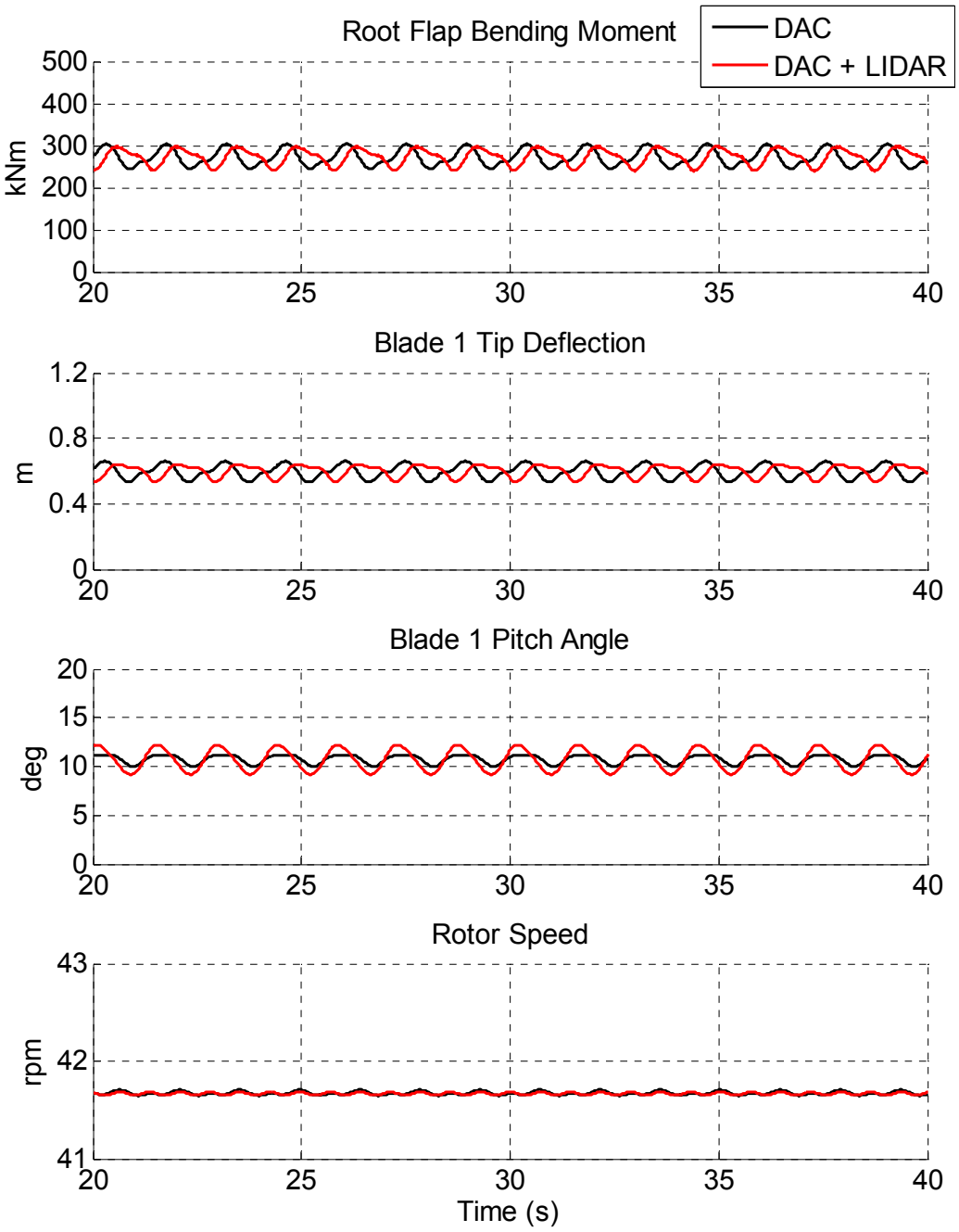

Figure 15. Simulated turbine operation with steady 18 m/s wind and power law shear exponent of 0.17

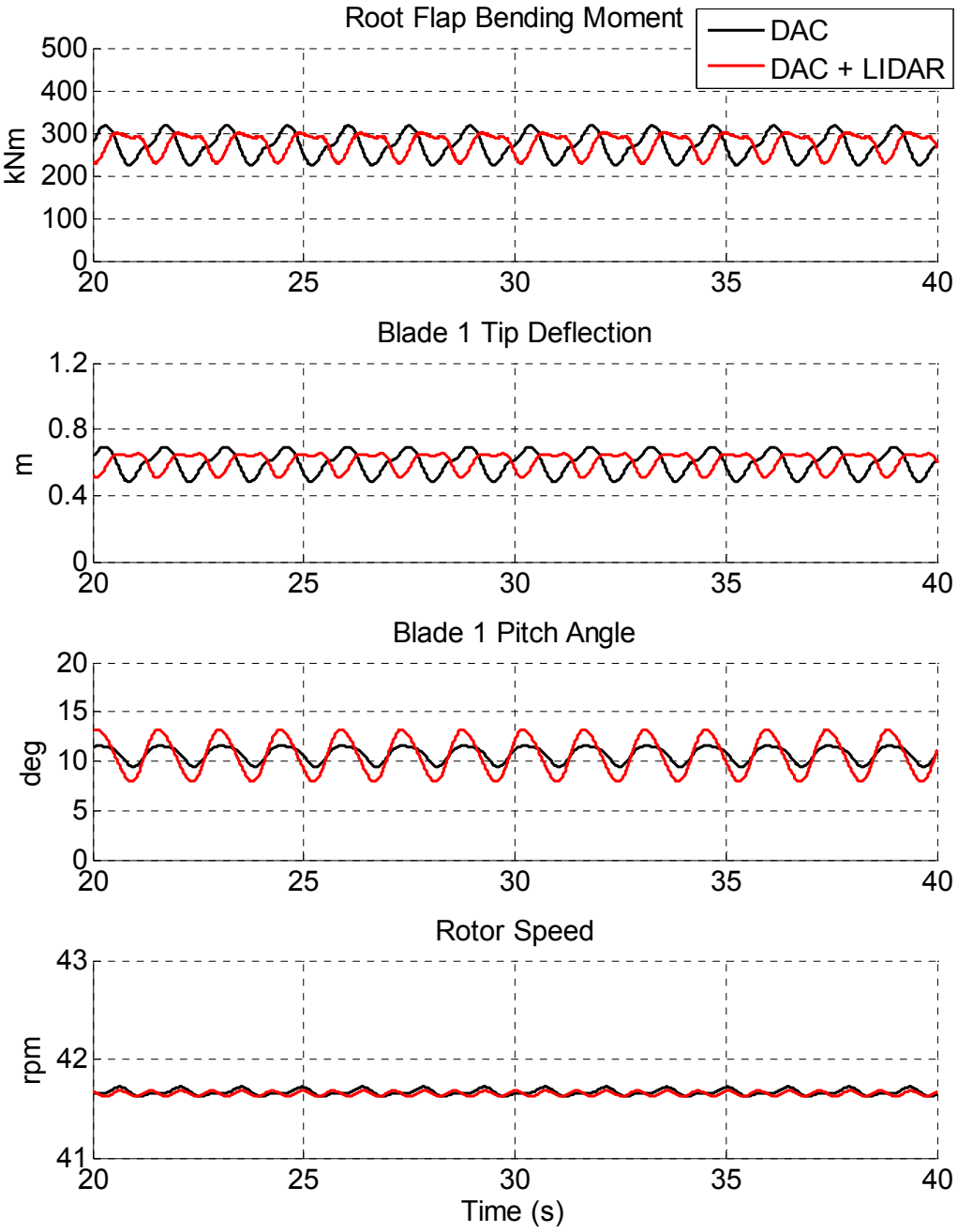

Figure 16. Simulated turbine operation with steady 18 m/s wind speed and power law shear exponent of 0.3

The simulation results for the two turbulent wind inflow cases are presented in Table 4. Again, speed regulation is achieved equally well for both controllers. With the turbulent flow field, the DAC + LIDAR controller reduced the blade flap DEL by 11% for the low shear case, and it is reduced by 10% for the high shear case when compared to the standard DAC controller. The peak bending moment is similar for both controllers. Corresponding time series of the bending moment, tip deflection, pitch angle, and rotor speed are shown in Figure 17 and Figure 18.

Table 4. Simulation Results for Turbulent Wind Conditions

	Turbulent 18 m/s wind, power law exponent = 0.17		Turbulent 18 m/s wind, power law exponent = 0.3	
	DAC	DAC + LIDAR	DAC	DAC + LIDAR
RMS speed error (rpm)	8.8	8.7	8.8	8.6
Max speed error (% of rated)	1.5	1.6	1.5	1.6
Blade 1 root flap bending moment DEL (kNm)	295	263	310	278
Blade 1 peak root flap bending moment (kNm)	467	464	475	475
Blade 1 root flap bending moment range (kNm)	466	400	480	421

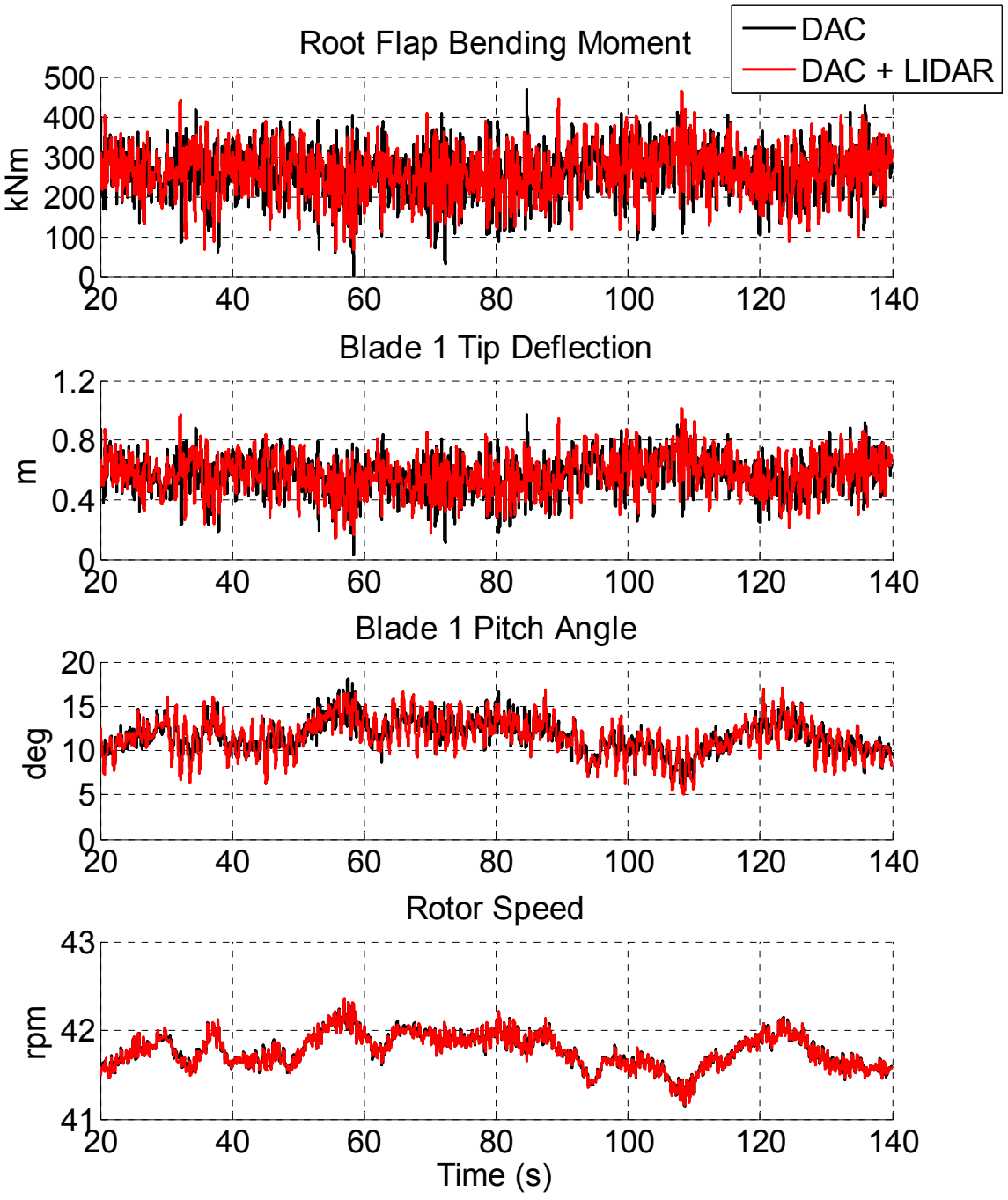

Figure 17. Simulated wind turbine operation for turbulent 18 m/s wind speed and average power law exponent of 0.17

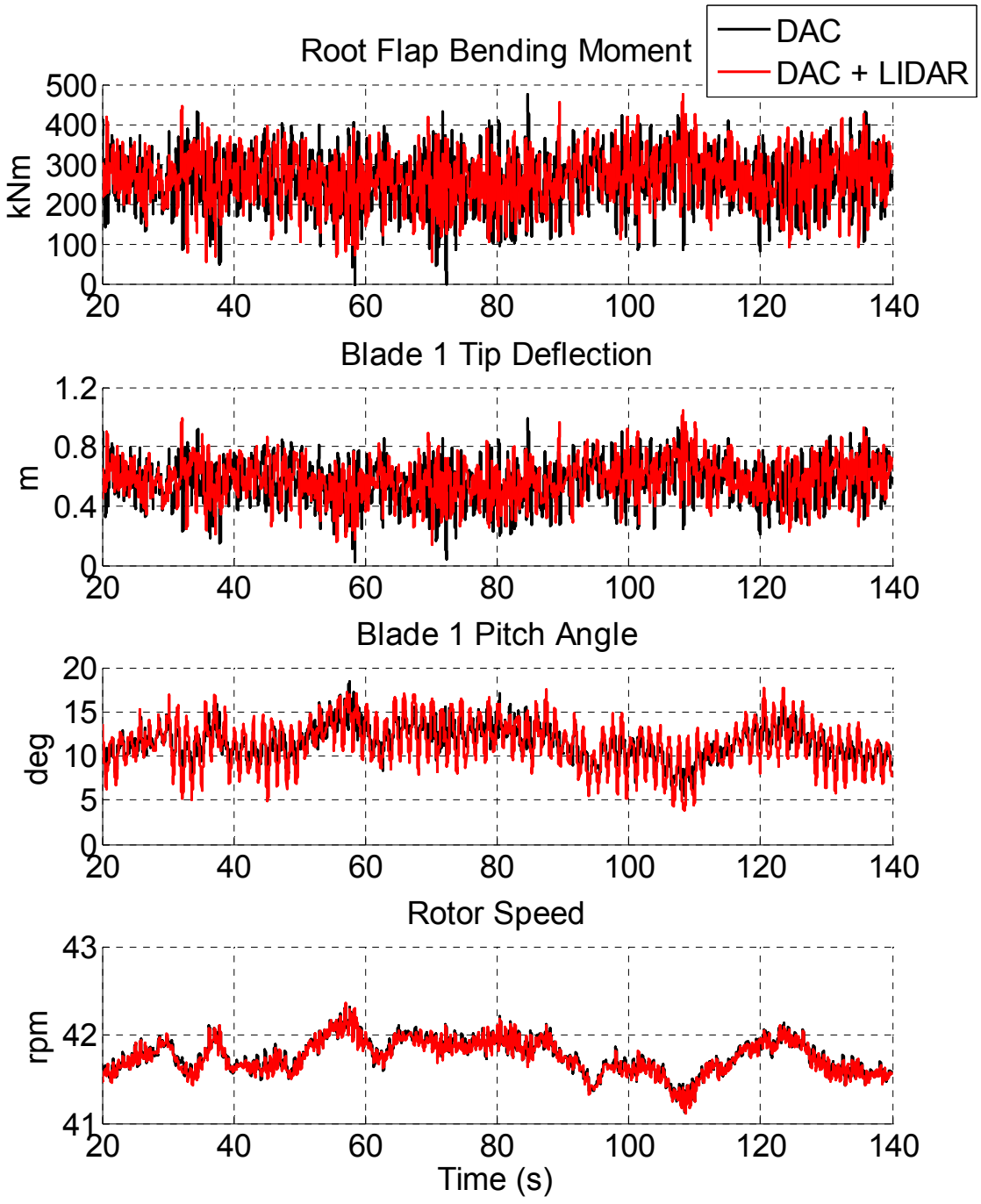

Figure 18. Simulated wind turbine operation for turbulent 18 m/s wind speed and power law shear exponent of 0.3

7.2 Conclusions

Inclusion of vertical shear measurements in wind turbine control for above-rated wind conditions appears to provide additional load mitigation capability over current state-of-the-art DAC. Damage equivalent flap loads were reduced by approximately 10% under turbulent wind inflow conditions when lidar signals were included as measurements to the controller. Additional components that must be considered include the drive train and tower. As the potential exists to reduce blade loads, it is reasonable to expect that lidar inputs to turbine controllers could serve to reduce loads on these other components as well.

The DAC controller requires measurements of the tip deflection of each blade for input to the controller. This type of measurement is not feasible for wind turbines, so this type of controller could not currently be implemented in the field. Some preliminary work has been done to use bending moment measurements as input to the controller because this type of measurement is possible to obtain. Because the lidar measurement is a feasible signal to add to controller inputs, the DAC + LIDAR controller could potentially be implemented.

Similarly, reduction in fatigue loading is only one aspect that will ultimately lead to design changes that result in cost of energy reductions. The loads resulting from extreme, discrete load cases that prescribe gusts and wind direction changes must also be reduced. Again, it is reasonable to expect that Lidar inputs to controllers could serve to reduce these extreme loads.

This simulation study was performed on a relatively small wind turbine by today's standards. The characteristics of lidar Configuration #1 are sufficient for this size of turbine. The focal distance of 1D is 43 m, which is easily achieved with Configuration #1. However, for a larger turbine exceeding 100 m in diameter, the extended focal distance of Configuration #2 may be required. Another consideration for application to larger turbines is the rotor speed. Very large turbines (rated at 5 MW), which are being considered by many turbine manufacturers, have rotation speeds of 12 rpm, which is significantly lower than the 42 rpm rotor speed in this study. Because the vertical shear computation is dependent on the rotor speed (Configuration #1 does not include internal scanning capability but relies on rotor rotation for scanning), slower speeds extend the time between measurements at the top and bottom of the rotor. This could result in a less accurate measurement of the vertical shear impinging on the rotor.

Finally, field testing is necessary to ascertain the effectiveness of including lidar-based controller inputs in wind turbine operation. Different operating regimes have different control objectives, and the transition between these regimes occurs frequently. It is only through field testing that these control systems can be thoroughly evaluated. Also, field testing is required to address concerns regarding the true correlation between upwind flow measurements and the turbine response. These differences cannot be simulated with current simulation capabilities.

8 Conclusions

The work presented here represents the first study (to our knowledge) that explores the potential of a turbine-mounted laser anemometer to enhance capabilities for wind energy production. The study has combined lidar know-how from QinetiQ with turbine design and control system expertise from the NWTC.

A number of cost-effective lidar options have been explored, and it has been shown that a system based on optical fiber operating at a wavelength close to 1.55μm will provide an economically viable solution. This technology is also well-proven, having been successfully deployed on the only two turbine-mounted lidar experiments of which we are aware.

The potential advantages of advance warning of wind speed fluctuations have been reviewed. One aspect has been examined in detail with a modelling study of a specific wind turbine control system, and the promising results obtained demonstrate the possible improvement in load mitigation. A full assessment of the advantages awaits further work on the remaining aspects identified in this study.

9 Recommendations and Proposed Future Work

9.1 Extensions to the Current Study

As a first study in the field of turbine-mounted lidar, this work has identified a number of areas for further research:

- There is a need for more modelling investigations to examine some of the other regimes listed in Figure 12. Controllers that include lidar-based wind measurement inputs must be specifically designed for each of the operating regimes.
- Eventually the modelling studies must extend to larger-scale turbines to provide a realistic estimate for the reduction in the COE. Current industry standard machines are rated at 1.5 MW with rotor diameters on the order of 80 m, but many companies are developing even larger turbines.
- It would be desirable to conduct experiments on turbine-mounted lidar in order to verify the results of the modelling work. Any scheme would ideally retain enough flexibility to explore different scan patterns and focus range options.
- The lidar experiments suggested above will also provide the capability for a wider range of investigations, including power curve measurement and turbine wake and shadowing studies.

9.2 Other Lidar Capabilities

We outline briefly two possible future lidar developments with potential for wind-energy-related research.

A three-axis scanned ground-based lidar system could examine wind field details for, e.g. turbine inflow. The main elements of such a system would be three lidar transceiver units, connected to a central rack and processing unit. Direction sensing is almost certainly required to resolve a six-fold ambiguity, adding considerable expense and complexity. The optimum baseline separation will depend on deployment details but will be of order 100 m. The three scanner units must ensure approximate coincidence in space of the three lidar foci (perfect overlap is not needed), from which the three components of wind speed (u, v, w) can be computed.

An additional option to be considered is a long-range pulsed system to provide information on 2D wind vector at any "point" in a volume of space out to ranges of 3-5 km. This would consist of two pulsed lidars on a baseline of ~1km. (Full 3D vector is not really possible because it is impractical to mount the third lidar in a location well outside the scan plane. QinetiQ has pioneered the use of dual-Doppler lidar for pollution dispersion studies and has several publications on the results of field trials and analysis of important issues [54]. While these studies used CO_2 laser sources (at a wavelength 10.6μm), we do not believe this technology provides an adequate solution to the current problem. Established 2μm lidars are well suited to this task, but it would also be possible to develop a system based on fiber/telecoms components at wavelength 1.5um. This would require some R&D to develop a laser source with the required pulse energy, repetition rate, and coherence properties; recent developments have been rapid in this area.

10 References/Bibliography

[1] Zak, J. A. *Atmospheric Boundary Layer Sensors forAapplication in a Wake Vortex Advisory System.* NASA/CR-2003-212175. Hanover, MD: NASA Scientific and Technical Information Program Office, April 2003.

[2] Durst, F.; Melling, A.; Whitelaw, J.H. *Principles and Practice of Laser Doppler Anemometry.* London: Academic Press, 1976.

[3] Adrian, R. J. "Particle-Imaging Techniques for Experimental Fluid Mechanics." *Ann. Rev. Fluid Mech;* Vol. 23**,** 1991; p. 261.

[4] Meyers, J. F. "Development of Doppler Global Velocimetry as a Flow Diagnostics Tool." *Meas, Sci. Technol;.* Vol. 6, 1995; p. 769.

[5] Canin, M. L.; Garnier, A.; Hauchecorne, A.; Porteneuve, J. "A Doppler Lidar for Measuring Winds in the Middle Atmosphere." *Geophys. Res. Lett.;* Vol. 16, 1989; p. 1273.

[6] Crescenti, G. H. "A Look Back on Two Decades of Doppler SODAR Comparison Studies." *Bull. Amer. Meteorol. Soc.;* Vol. 78, 1997; pp. 651-673.

[7] Constant, G.; Foord, R.; Forrester, P.A.; Vaughan, J.M. "Coherent Laser Radar and the Problem of Aircraft Wake Vortices." *Journal of Modern Optics;* Vol. 41, 1994; pp. 2153-2173.

[8] Harris, M.; Young, R.I.; Köpp, F.; Dolfi, A.; Cariou, J-P. "Wake Vortex Detection and Monitoring." *Aerospace Science and Technolog*y; Vol. 6, 2002; pp. 325-331.

[9] Karlsson, C.; Olsson, F.; Letalick, D.; Harris, M. "All-Fiber Multifunction CW 1.55 Micron Coherent Laser Radar for Range, Speed, Vibration and Wind Measurements." *Applied Optics;* Vol. 39, 2000; pp. 3716-3726.

[10] Sonnenschein, C. M.; Horrigan, F.A. "Signal-to-Noise Relationships for Coaxial Systems that Heterodyne Backscatter from the Atmosphere." *Appl. Opt.;* Vol. 10, 1971; pp. 1600-1604.

[11] Pearson, G. N.; Collier, C.G. "A Pulsed Coherent CO_2 Lidar for Boundary-Layer Meteorology." *Q. J. R. Meteorol. Soc.;* Vol. 125, 1999; pp. 2703-2721.

[12] Pearson, G. N.; Roberts, P.J.; Eacock, J.R.; Harris, M. "Analysis of the Performance of a Coherent Pulsed Fiber Lidar for Aerosol Backscatter Applications." *Applied Optics;* Vol. 41, 2002; pp. 6442-6450.

[13] International Electrotechnical Commission (IEC). 2001. *Safety of Laser Products – Part 1: Equipment Classification, Requirements, and User's Guide.* IEC 60825-1 (2001 Revision).

[14] Jelalian, A. V. *Laser Radar Systems.* Boston: Artech House, 1992.

[15] Vaughan, J. M.; Steinvall, K.O.; Werner, C.; Flamant, P.H. "Coherent Laser Radar in Europe." *Proceedings of the IEEE;* Vol. 84, Issue 2, Feb. 1996; pp. 205.

[16] Harris, M.; Constant, G.; Ward, C. “Continuous-Wave Bistatic Laser Doppler Wind Sensor.” *Appl. Opt.;* Vol. 40**,** 2001; pp. 1501-1506.

[17] Jørgensen, H.; Mikkelsen, T.; Mann, J.; Bryce, D.; Coffy, A.; Harris, M.; and Smith, D. “Site Wind Field Determination Using a CW Doppler Lidar - Comparison with Cup Anemometers at Risø.” *Proc. EWEA Special Topic Conference: The Science of Making Torque from Wind; April 19-21, 2004*, *Delft, The Netherlands.* pp.261-266.

[18] Smith, D.; Harris, M.; Coffey, A.; Mikkelsen, T.; Jørgensen, H.; Mann, J.; and Danielian, R. “Wind Lidar Evaluation at the Danish Wind Test Site in Høvsøre *Proceedings of the 2004 European Wind Energy Conference; November 22-25, 2004, London.*

[19] Antoniou, I.; Jørgensen, H.; Mikkelsen, T.; Pedersen, T.; Warmbier, G.; and Smith, D. “Comparison of Wind Speed and Power Curve Measurements Using a Cup Anemometer, a Lidar and a Sodar.” *Proceedings of the 2004 European Wind Energy Conference; November 22-25, 2004, London.*

[20] Harris, M.; Bryce, D.; Coffey, A.; Smith, D.; Birkemeyer, J.; Knopf, U. “Advance Measurements of Gusts by Laser Anemometry.” *Submitted to Journal of Wind Engineering and Industrial Aerodynamics*, June 2004.

[21] Bingöl, F. “Adapting a Doppler Laser Anemometer to Wind Energy.” (2005). Masters thesis online, http://www.afm.dtu.dk/Publications/msc.html. Last modified Feb. 6, 2005; accessed Dec. 13, 2005.

[22] Banakh, V. A.; Smalikho, I.N.; Köpp, F.; Werner, C. "Representativeness of Wind Measurements with a CW Doppler Lidar in the Atmospheric Boundary Layer." *Applied Optics;* Vol. 34, 1993; pp. 2055-2067.

[23] Hardesty, R. M.; Weber, B.F. “Lidar Measurement of Turbulence Encountered by Horizontal-Axis Wind Turbines.,” *J Atm. and Oceanic Tech.;* Vol. 4, 1987; p. 191.

[24] Vaughan, J. M.; Forrester, P.A. “Laser Doppler Velocimetry Applied to the Measurement of Local and Global Wind.” *Wind Engineering;* Vol. 13, 1989; p. 1.

[25] Hill, C.; Harris, M.; Ridley, K.; Jakeman, E.; and Lutzmann, P. “Lidar Frequency Modulation Vibrometry in the Presence of Speckle.” *Applied Optics;* Vol. 42, 2003; p. 1091.

[26] Jonkman, B.; Buhl Jr., M.L. “TurbSim User’s Guide,” NREL/EL-500-36970. Golden, CO: National Renewable Energy Laboratory, September 2005.

[27] Wilson, R.E.; Freeman, L.N.; Walker, S.N.; Harman, C.R. *Final Report for the FAST Advanced Dynamics Code: Two Bladed Teetered Hub Version 2.4 User's Manual Appendix for Three and Four Bladed Versions.* NREL/SR-500-23563, Golden, CO: National Renewable Energy Laboratory, 1996.

[28] Jonkman, J. M.; Buhl Jr., M. L. *FAST User's Guide.* NREL/EL-500-29798. Golden, CO: National Renewable Energy Laboratory, 2005.

[29] Kelley N.; Hand, M.; Larwood, S.; McKenna, E. “The NREL Large-Scale Turbine Inflow and Response Experiment – Preliminary Results.” *Collection of the 2002 ASME Wind Energy Symposium Technical Papers Presented at the 40th AIAA Aerospace Sciences Meeting and Exhibit, January 14-17, 2002, Reno, Nevada.* New York: American Society of Mechanical Engineers (ASME), 2002; pp. 412-426.

[30] Malcolm, D.J.; Hansen, A.C. *WindPACT Turbine Rotor Design Study: June 2000–June 2002*. NREL/SR-500-32495. Golden, CO: National Renewable Energy Laboratory, 2002.

[31] Sutherland, H.J. *On the Fatigue Analysis of Wind Turbines.* SAND99-0089. Albuquerque, NM: Sandia National Laboratories, 1999.

[32] Fragoulis, A.N. (1997). "The Complex Terrain Wind Environment and Its Effects on the Power Output and Loading of Wind Turbines." *Collection of the 1997 ASME Wind Energy Symposium Technical Papers Presented at the 35th AIAA Aerospace Sciences Meeting and Exhibit, January 6-9, Reno, Nevada.* New York: American Society of Mechanical Engineers (ASME); pp. 33–40.

[33] Glinou, G.; Fragoulis, A., eds. *Mounturb Final Report.* 3 vols., JOU2-CT93-0378. Pikermi, Greece: Center for Renewable Energy Sources Wind Energy Department (CRES.WE), 1996.

[34] Sutherland, H. (2002). "Inflow and the Fatigue of the LIST Wind Turbine." *Collection of the 2002 ASME Wind Energy Symposium Technical Papers Presented at the 40th AIAA Aerospace Sciences Meeting and Exhibit, January 14-17, Reno, Nevada.* New York: American Society of Mechanical Engineers (ASME); pp. 427-437.

[35] Rice, R., ed. *SAE Fatigue Design Handbook.* 3rd edition. Warrendale, PA: Society of Automotive Engineers, 1997; 470 pp.

[36] Moriarty, P. J.; Hansen, A. C. *AeroDyn Theory Manual.* NREL/TP-500-36881. Golden, CO: National Renewable Energy Laboratory, 2005.

[37] Laino, D.J. "Aerodyn." NWTC Design Codes online, http://wind.nrel.gov/designcodes/simulators/aerodyn/. Last modified July 5, 2005; accessed July 5, 2005.

[38] Johnson, K.; Fingersh, L. J.; Wright, A. *Controls Advanced Research Turbine: Lessons Learned during Advanced Controls Testing.* NREL/TP-500-38130. Golden, CO: National Renewable Energy Laboratory, 2005.

[39] Fingersh, L. J.; Johnson, K. E. "Baseline Results and Future Plans for the NREL Controls Advanced Research Turbine." *Collection of the 2004 ASME Wind Energy Symposium Technical Papers at the 42nd AIAA Aerospace Sciences Meeting and Exhibit, January 5-8, 2004, Reno, Nevada.* New York: American Institute of Aeronautics and Astronautics, Inc. (AIAA) and American Society of Mechanical Engineers (ASME); pp. 87-93.

[40] Fingersh, L. J.; Johnson, K. *Controls Advanced Research Turbine (CART) Commissioning and Baseline Data Collection.* NREL/TP-500-32879. Golden, CO: National Renewable Energy Laboratory, 2002.

[41] Wright, A. D.; Stol, K. A.; Fingersh, L. J. "Progress in Implementing and Testing State-Space Controls for the Controls Advanced Research Turbine." AAIA-2005-0395. *Collection of the 2005 ASME Wind Energy Symposium Technical Papers at the 42nd AIAA Aerospace Sciences Meeting and Exhibit, January 10-13, 2005, Reno, Nevada.* New York: American Institute of Aeronautics and Astronautics, Inc. (AIAA) and American Society of Mechanical Engineers (ASME); pp. 88-100.

[42] Johnson, K. E.; Fingersh, L. J.; Pao, L. Y.; Balas, M. J. "Adaptive Torque Control of Variable Speed Wind Turbines for Increased Region 2 Energy Capture." AIAA-2005-0392. *Collection of the 2005 ASME Wind Energy Symposium Technical Papers at the 42nd AIAA Aerospace Sciences Meeting and Exhibit, January 10-13, 2005, Reno, Nevada.* New York: American Institute of Aeronautics and Astronautics, Inc. (AIAA) and American Society of Mechanical Engineers (ASME); pp. 66-76.

[43] Johnson, K. E.; Fingersh, L. J.; Balas, M. J.; Pao, L. Y. (2004). "Methods for Increasing Region 2 Power Capture on a Variable-Speed Wind Turbine." *Journal of Solar Energy Engineering: Transactions of the ASME.* Vol. 126, 2004; pp. 1092-1100.

[44] Stol, K. A.; Fingersh, L. J. *Wind Turbine Field Testing of State-Space Control Designs: August 25, 2003-November 30, 2003.* NREL/SR-500-35061. Golden, CO: National Renewable Energy Laboratory, 2004.

[45] Wright, A. D. *Modern Control Design for Flexible Wind Turbines.* NREL/TP-500-35816. Golden, CO: National Renewable Energy Laboratory, 2004.

[46] Wright, A. D.; Balas, M. J. (2004). "Design of Controls to Attenuate Loads in the Controls Advanced Research Turbine." *Journal of Solar Energy Engineering: Transactions of the ASME.* Vol. 126, 2004; pp. 1083-1091.

[47] Wright, A. D.; Balas, M. J. (2003). "Design of State-Space-Based Control Algorithms for Wind Turbine Speed Regulation." *Journal of Solar Energy Engineering: Transactions of the ASME* . Vol. 125, 2003; pp. 386-395.

[48] Hand, M. M. *Mitigation of Wind Turbine/Vortex Interaction Using Disturbance Accommodating Control.* NREL/TP-500-35172. Golden, CO: National Renewable Energy Laboratory, 2003.

[49] Stol, K. A. "Disturbance Tracking Control and Blade Load Mitigation for Variable-Speed Wind Turbines." *Journal of Solar Energy Engineering: Transactions of the ASME.* Vol. 125, 2003; pp. 396-401.

[50] Stol, K. A.; Balas, M. J. "Periodic Disturbance Accommodating Control for Blade Load Mitigation in Wind Turbines." *Journal of Solar Energy Engineering: Transactions of the ASME.* Vol. 125, 2003; pp. 379-385.

[51] Stol, K.; Balas, M. "Full-State Feedback Control of a Variable-Speed Wind Turbine: A Comparison of Periodic and Constant Gains." *Journal of Solar Energy Engineering: Transactions of the ASME.* Vol. 123, 2001; pp. 319-326.

[52] Johnson, C.D. (1976). "Theory of Disturbance Accommodating Controllers." Leondes, C.T., ed. *Control and Dynamic Systems: Advances in Theory and Applications,* Vol. 12. New York: Academic Press; pp. 387-489.

[53] Kelley, N.; Shirazi, M.; Jager, D.; Wilde, S.; Adams, J.; Buhl, M.; Sullivan, P.; Patton, E. *Lamar Low-Level Jet Project Interim Report*. NREL/TP-500-34593. Golden, CO: National Renewable Energy Laboratory, January 2004.

[54] Collier, C.; Davies, F.; Bozier, K.; Holt, A.; Middleton, D.; Pearson, G.; Siemen, S.; Willetts, D.; Upton, G.; and Young, R. "Dual Doppler Lidar Measurements for Improving Dispersion Models." *Bull. Am. Met. Soc.;* Vol. 86, 2005; p. 825.

A Appendix: Abbreviations and Definitions

ADC	analog-to-digital converter
AOM	acousto-optic modulator
CART	Controls Advanced Research Turbine
CLR	coherent laser radar
CDL	coherent Doppler lidar (n.b. CLR, CDL, and "reference beam LDA" are precisely equivalent)
COE	cost of energy
CW	continuous wave
DAC	disturbance accommodating controller
DEL	damage equivalent load
DFT	digital (or discrete) Fourier transform
DGV	Doppler global velocimetry
DIAL	differential absorption lidar
FFT	fast Fourier transform
FPGA	field programmable gate array
LDA	laser Doppler anemometry
LDV	laser Doppler velocimetry
LO	local oscillator
LWST	Low Wind Speed Technologies
MPE	maximum permissible exposure
MIMO	multiple-input-multiple-output
PIV	particle imaging velocimetry
PM	polarization maintaining
RMS	root mean square
SAW	surface acoustic wave
SBS	stimulated Brillouin scattering
SNR	signal-to-noise ratio
λ	lidar wavelength
ν	laser frequency
$\delta\nu$	Doppler frequency shift
V_{LOS}	line-of-sight component of wind velocity
P_T	transmitted laser power
P_S	received signal power
$\beta(\pi)$	backscatter coefficient
Γ	half-width at half height of lidar axial sensitivity function
x	horizontal direction along turbine axis (+ve x in upwind direction)
y	horizontal direction perpendicular to turbine axis
z	vertical direction
V_C	centroid velocity of a given spectrum
F	axial lidar sensitivity weighting function
A	beam radius at lidar output (to $1/e^2$ in intensity)
R	distance from lidar aperture to beam focus
Δ	distance from focus along beam direction
θ	off-axis angle for lidar device, deg
h	wind turbine hub height, m
i	number of cycle counting bins
m	material constant, exponent for the S-N curve (10 for fiberglass composite material), or vertical wind shear exponent

n	number of rain-flow cycles in the ith bin
u,v,w	wind velocity components corresponding to x, y, z coordinates, respectively, m/s
x,y,z	blade element coordinates in aerodynamic code coordinate system, m
z_g	height above ground level, m
F_i	amplitude of the ith cycle counting bin, kNm
F_e	equivalent fatigue load, kNm
N_o	cycles over 10-minute period (840)
W	wind speed, m/s

B Appendix: Table of ZephIR Specifications

This table lists the essential specifications of the ZephIR production instrument. These provide an accurate representation of the expected requirements of a turbine-mounted lidar system.

Wavelength	1.55 μm
Output power	Up to 1 Watt
Telescope aperture diameter	72 mm
Focus range	from 5 m to 200 m
Detector	InGaAs photodiode
Sample rate	100 MHz
FFT size	512, giving 256 bins in 50 MHz spectrum
Number of spectral averages	4000
Minimum detectable wind speed	0.14 m s^{-1}
Maximum detectable wind speed	38.7 m s^{-1}
Bin size (velocity resolution)	0.15 m s^{-1}
Data rate	~50 measurements per second

REPORT DOCUMENTATION PAGE

Form Approved
OMB No. 0704-0188

PLEASE DO NOT RETURN YOUR FORM TO THE ABOVE ORGANIZATION.

1. REPORT DATE *(DD-MM-YYYY)*	2. REPORT TYPE	3. DATES COVERED *(From - To)*
January 2006	Technical Report	3/1/05 - 11/30/05

4. TITLE AND SUBTITLE
Lidar for Turbine Control: March 1, 2005 – November 30, 2005

5a. CONTRACT NUMBER
DE-AC36-99-GO10337

5b. GRANT NUMBER

5c. PROGRAM ELEMENT NUMBER

6. AUTHOR(S)
M. Harris, M. Hand, A. Wright

5d. PROJECT NUMBER
NREL/TP-500-39154

5e. TASK NUMBER
WER6.0301

5f. WORK UNIT NUMBER

7. PERFORMING ORGANIZATION NAME(S) AND ADDRESS(ES)
QinetiQ, Inc., P.O. Box 4365, Philadelphia, PA 19118
National Renewable Energy Laboratory, 1617 Cole Blvd.
Golden, CO 80401-3393

8. PERFORMING ORGANIZATION REPORT NUMBER
YAM-5-33200-11
NREL/TP-500-39154

9. SPONSORING/MONITORING AGENCY NAME(S) AND ADDRESS(ES)

10. SPONSOR/MONITOR'S ACRONYM(S)
NREL

11. SPONSORING/MONITORING AGENCY REPORT NUMBER

12. DISTRIBUTION AVAILABILITY STATEMENT
National Technical Information Service
U.S. Department of Commerce
5285 Port Royal Road
Springfield, VA 22161

13. SUPPLEMENTARY NOTES
NREL Technical Monitor: S. Schreck

14. ABSTRACT *(Maximum 200 Words)*
This work represents the first study (to our knowledge) that explores the potential of a turbine-mounted laser anemometer to enhance capabilities for wind energy production. The study combines laser anemometry (lidar) know-how from QinetiQ, Malvern, United Kingdom, with turbine design and control system expertise from the National Wind Technology Center (NWTC) at the National Renewable Energy Laboratory (NREL), Colorado, United States of America.

15. SUBJECT TERMS
wind energy; lidar; laser anemometry; wind speed measurement

16. SECURITY CLASSIFICATION OF:			17. LIMITATION OF ABSTRACT	18. NUMBER OF PAGES	19a. NAME OF RESPONSIBLE PERSON
a. REPORT	b. ABSTRACT	c. THIS PAGE			19b. TELEPHONE NUMBER (*Include area code*)
Unclassified	Unclassified	Unclassified	UL		

Standard Form 298 (Rev. 8/98)
Prescribed by ANSI Std. Z39.18